

# CANADIAN THESES ON MICROFICHE

I.S.B.N.

# THESES CANADIENNES SUR MICROFICHE



National Library of Canada  
Collections Development Branch

Canadian Theses on  
Microfiche Service

Ottawa, Canada  
K1A 0N4

Bibliothèque nationale du Canada  
Direction du développement des collections

Service des thèses canadiennes  
sur microfiche

## NOTICE

The quality of this microfiche is heavily dependent upon the quality of the original thesis submitted for microfilming. Every effort has been made to ensure the highest quality of reproduction possible.

If pages are missing, contact the university which granted the degree.

Some pages may have indistinct print especially if the original pages were typed with a poor typewriter ribbon or if the university sent us a poor photocopy.

Previously copyrighted materials (journal articles, published tests, etc.) are not filmed.

Reproduction in full or in part of this film is governed by the Canadian Copyright Act, R.S.C. 1970, c. C-30. Please read the authorization forms which accompany this thesis.

THIS DISSERTATION  
HAS BEEN MICROFILMED  
EXACTLY AS RECEIVED

## AVIS

La qualité de cette microfiche dépend grandement de la qualité de la thèse soumise au microfilmage. Nous avons tout fait pour assurer une qualité supérieure de reproduction.

S'il manque des pages, veuillez communiquer avec l'université qui a conféré le grade.

La qualité d'impression de certaines pages peut laisser à désirer, surtout si les pages originales ont été dactylographiées à l'aide d'un ruban usé ou si l'université nous a fait parvenir une photocopie de mauvaise qualité.

Les documents qui font déjà l'objet d'un droit d'auteur (articles de revue, examens publiés, etc.) ne sont pas microfilmés.

La reproduction, même partielle, de ce microfilm est soumise à la Loi canadienne sur le droit d'auteur, SRC 1970, c. C-30. Veuillez prendre connaissance des formules d'autorisation qui accompagnent cette thèse.

LA THÈSE A ÉTÉ  
MICROFILMÉE TELLE QUE  
NOUS L'AVONS REÇUE



60265

### PERMISSION TO MICROFILM — AUTORISATION DE MICROFILMER

Please print or type — Écrire en lettres moulées ou dactylographier

Full Name of Author — Nom complet de l'auteur

GEORGE KOVAR

Date of Birth — Date de naissance

DECEMBER 4<sup>th</sup> 1956

Country of Birth — Lieu de naissance

PRAGUE, CZECHOSLOVAKIA

Permanent Address — Résidence fixe

89 WOODFIELD DR, NEPEAN ONTARIO, K2G 0A1

Title of Thesis — Titre de la thèse

OPTICAL AND FOURIER TECHNIQUES FOR GEOPHYSICAL STRAIN MEASUREMENTS

University — Université

ALBERTA

Degree for which thesis was presented — Grade pour lequel cette thèse fut présentée

MSC

Year this degree conferred — Année d'obtention de ce grade

FALL 1982

Name of Supervisor — Nom du directeur de thèse

EDO NYLAND

Permission is hereby granted to the NATIONAL LIBRARY OF CANADA to microfilm this thesis and to lend or sell copies of the film.

L'autorisation est, par la présente, accordée à la BIBLIOTHÈQUE NATIONALE DU CANADA de microfilmer cette thèse et de prêter ou de vendre des exemplaires du film.

The author reserves other publication rights, and neither the thesis nor extensive extracts from it may be printed or otherwise reproduced without the author's written permission.

L'auteur se réserve les autres droits de publication; ni la thèse ni de longs extraits de celle-ci ne doivent être imprimés ou autrement reproduits sans l'autorisation écrite de l'auteur.

Date

June 2 1982

Signature

George Kovar

THE UNIVERSITY OF ALBERTA

Optical and Fourier Techniques for Geophysical Strain  
Measurements

by



George Kovar

A THESIS

SUBMITTED TO THE FACULTY OF GRADUATE STUDIES AND RESEARCH  
IN PARTIAL FULFILMENT OF THE REQUIREMENTS FOR THE DEGREE  
OF Master of Science

Physics

EDMONTON, ALBERTA

Fall 1982

THE UNIVERSITY OF ALBERTA

RELEASE FORM

NAME OF AUTHOR           George Kovar  
TITLE OF THESIS         Optical and Fourier Techniques for  
                              Geophysical Strain Measurements  
DEGREE FOR WHICH THESIS WAS PRESENTED   Master of Science  
YEAR THIS DEGREE GRANTED   Fall 1982

Permission is hereby granted to THE UNIVERSITY OF ALBERTA LIBRARY to reproduce single copies of this thesis and to lend or sell such copies for private, scholarly or scientific research purposes only.

The author reserves other publication rights, and neither the thesis nor extensive extracts from it may be printed or otherwise reproduced without the author's written permission.

(SIGNED) .. *George Kovar* .....

PERMANENT ADDRESS:

..... *89 WOODFIELD DR.* .....  
..... *NEPEAN, ONTARIO* .....  
..... *K2G 0A1* .....

DATED ..... *May 28* ..... 1982

THE UNIVERSITY OF ALBERTA  
FACULTY OF GRADUATE STUDIES AND RESEARCH

The undersigned certify that they have read, and recommend to the Faculty of Graduate Studies and Research, for acceptance, a thesis entitled Optical and Fourier Techniques for Geophysical Strain Measurements submitted by George Kovar in partial fulfilment of the requirements for the degree of Master of Science.

.....*Edo Gryn*.....  
Supervisor

.....*J. E. Samson*.....  
.....*D. P. Hevins*.....  
.....*Robert Ledosjevics*.....

Date.....*May 28*.....*1982*.....

## Abstract

One problem central to the study of slow deformation of the ground is its accurate measurement. Traditional techniques, repeated high precision surveys, tilt meter observations and strain meter observations suffer firstly from expense, difficult field procedure and low productivity and secondly from the problem of extrapolating measurements made at a single point on the earth's surface to a measure of average behaviour over a larger area. It may be possible to make estimates of strain changes in photographic records of the ground at different times, using commercially available photogrammetric equipment, combined with a commercially available frequency analysing optical set-up. Preliminary calculations show that it is possible to detect a differential ground displacement of 1cm, using a simple optical filtering technique for the analysis of the photographs.

### Acknowledgements

I would like to express my appreciation to my supervisor, Dr. E. Nyland, for initially suggesting this topic, and for his assistance during the study.

I wish to thank Dr. J. Samson, for his careful review of this thesis, and for his guidance during Dr. Nyland's absence.

Most of all, I would like to express my thanks to my parents, for their continuous support, and to my friends, for making my two year stay in a strange city an enjoyable one.

I acknowledge the support of the University of Alberta in the form of a teaching assistantship.

## Table of Contents

Chapter	Page
1. INTRODUCTION .....	1
1.1 EDM Accuracy .....	8
2. IMAGING SYSTEMS .....	16
2.1 Lenses .....	17
2.2 Effects of coherence on imaging systems .....	20
2.3 Optical Processing .....	23
2.4 Atmosphere .....	29
2.5 Optical monitoring of surface deformations .....	31
2.6 Preliminary Calculations .....	38
3. INTERFEROMETRIC COMPARISON OF TRANSPARENCIES .....	42
3.1 Recording a random pattern .....	45
3.2 Whole field filtering .....	49
3.3 Pointwise filtering .....	52
3.4 The Discrete Fourier Transform .....	58
4. COMPUTATIONS WITH SYNTHETIC DATA .....	63
5. CONCLUSION .....	82
5.1 Suggestion for geophysical experiment .....	84
BIBLIOGRAPHY .....	88
APPENDIX A: Notation .....	94
APPENDIX B: Proofs of Fourier Transform Theorems .....	95
APPENDIX C: Programs .....	98



## List of Figures

Figure 1....Performance of the Sokkisha EDM under windy conditions. 0 seconds corresponds to 2:40 pm. page 9

Figure 2....Difference between distance measurements of the SOKKISHA and HP3800 infrared EDM units. 70% of the points lie between  $\pm\sigma$ ; 97% lie between  $\pm 2\sigma$ . page 11

Figure 3....Fall-off of return signal with decreasing reflector surface area for three different distances for the HP3800 page 13

Figure 4....The return signal reaching the instrument pointed a distance  $D$  away from the reflector of radius  $R$ , 1290 meters away. Spreading of the beam is therefore about 0.001 radians. page 14

Figure 5....Object with complex amplitude distribution  $g$ , is placed in front of a convex thin spherical lens of focal length  $f$ . The resulting amplitude distribution is  $g_1$ . page 18

Figure 6....Image of a sharp edge: Intensity as a function of distance perpendicular to the edge. Dashed line represents coherent illumination; solid line represents incoherent illumination of the edge page 22

- Figure 7....Arrangement of an optical Fourier analyser  
page 25
- Figure 8....Above: side view of the path followed by the rays from point P to the camera at C. Below: top view - distance  $s$  split up into its components parallel and perpendicular to the fault.  
page 36
- Figure 9....Recording a random pattern  
page 46
- Figure 10....Arrangement for pointwise filtering  
page 53
- Figure 11....Development of the discrete Fourier transform pair: figure taken from Brigham, 1974, p95  
page 59
- Figure 12....A triangle function sampled at different rates, with its discrete Fourier transform on the right  
page 62
- Figure 13....For a peak of width 1, fringes extend to infinity  
page 64
- Figure 14....Displacement is inversely proportional to the fringe separation  
page 65
- Figure 15....Calibration graph showing inverse relationship between fringe separation and distance between the peaks  
page 66

Figure 16....A displacement of  $d=0$  produces the diffraction halo, the frequency distribution due to a single peak

page 68

Figure 17....Fringes become visible only when  $d > 16$ , as predicted by equation 3.23

page 69

Figure 18....Differences in diffraction patterns for  $d=40$  and  $d=41$  can be easily measured with a ruler

page 70

Figure 19....Fringes are still clearly visible when random noise is added to the signal

page 71

Figure 20....Amplitude of noise has been reduced by band-pass filtering, with no significant improvement in the visibility of fringes

page 72

Figure 21....Signal to noise ratio is reduced; fringes are still visible

page 73

Figure 22....At high noise level, band-pass filtering again has no effect on fringe visibility

page 74

Figure 23....Radius of the diffraction halo decreases with increasing peak width. In this figure, the peak is 50 lines wide.

page 75

Figure 24....If one peak is wider than the other, the size of the halo is limited by the width of the wider peak: width of peak shown is 50, other peak has a width of 18 page 77

Figure 25....A beat pattern is observed if two lights are present in one section page 79

Figure 26....Interference pattern obtained from a random pattern of delta functions page 80

Figure 27....Density plot of a diffraction pattern produced by 2 gaussian-shaped peaks showing the orientation and magnitude the displacement. The actual displacement was  $d=(48,40)$ . page 81

## 1. INTRODUCTION

Prediction of occurrence of large earthquakes requires careful monitoring of the accumulation of stress and strain along major faults.

According to the theory of plate tectonics, the earth's crust consists of a number of brittle plates. Due to their large size, these plates will exhibit elastic behaviour, in spite of their relatively high shear strength. The plates are driven across the asthenosphere with relative speeds up to 12 cm/year. Usually, the motion along a plate boundary is continuous, through aseismic creep, however portions of some boundaries may become locked, with little relative motion taking place. Stress accumulates on a locked fault, until it reaches a critical value, known as the failure stress. When the failure stress is reached, the contact zone ruptures, causing an earthquake, accompanied by a sudden displacement, which releases the accumulated stress.

We expect that due to plastic deformation, the fault will be locked only to a certain depth  $h$ , below which the motion will be continuous. Turcotte and Spence (1974) made the following simplifications, which enabled them to model the strain accumulation along a locked strike slip fault:

1. The depth  $h$  is constant along the fault.
2. There is zero friction below this depth.
3. The base of each plate is at a constant depth  $H$ , and is free to slide over the asthenosphere.

Using these simplifications, the authors derived the

displacement field at the surface, the mean stress on the fault plane as a function of time, and the rate at which energy is stored in the system.

The driving mechanism of plates is associated with forces extending across the entire plate. Frictional forces acting on the sides of the plates balance part of the driving forces. The accumulation of stresses associated with these forces prior to an earthquake only extends a distance  $q$  into the plate, where  $q$  is the typical dimension of the fault break associated with a strike slip earthquake.

Observations of surface deformations are thus of vital importance to the understanding of earthquake mechanisms. Due to the slow rates of strain accumulation near faults, measurements with a precision of at least 1 part per million are necessary, if the observations are to be completed in one or two years.

Satellite laser-ranging techniques have reached a stage where distances between two points on the earth can be determined to within a few centimeters, and are therefore excellent tools for determining motion on a large scale (50 km or more). At present, the main source of error is the motion of the spacecraft, which is affected by gravity anomalies.

For distances shorter than ten km, ground-based geodetic techniques are the principal means of deformation monitoring. In 1973, Savage and Prescott showed one can

attain the required accuracy in a single measurement, using a Geodolite, an electronic distance measuring unit (EDM).

A Geodolite produces a modulated laser beam, which is reflected back to the instrument by a distant retroreflector. The instrument then compares the modulation phases of the incoming and outgoing beams, which determines the optical path in terms of an unknown number of whole modulation wavelengths, plus a fraction of a wavelength. This fraction can be precisely measured, and the number of whole wavelengths is determined by repeating the measurement at successively lower modulation frequencies. The stability of the modulation frequency will give the limit of accuracy of the instrument.

In practice however, the accuracy with which we can determine the path length, or make any optical measurement, will depend on the accuracy of the measurement of the refractive index of air, ( $n$ ) through which the beam passes. The spectrum of fluctuations in  $n$  shows significant power from periods of a few milliseconds up to very long periods, measured in days (Slater, 1975). It is reasonable to assume that long-period fluctuations are caused by weather changes which affect very large areas, and short-period fluctuations are caused by atmospheric turbulence, affecting very small areas (having high spatial frequency components). In the Savage-Prescott experiments, the high frequency fluctuations in  $n$  are eliminated by 1-or 10-second signal averaging built into the geodolite. To eliminate intermediate and long

frequency fluctuations, it is necessary to measure the humidity, temperature and pressure along the line of sight. The accuracy with which these measurements are made will limit the precision of the distance measurement.

Savage and Prescott made these measurements by use of an aircraft with a probe mounted on each side (on wing struts of an airplane or skids of a helicopter). Repeated measurements were taken during the flight, to eliminate intermediate frequency fluctuations. Pressure was measured at the two end points of the line. Since the accuracy of the measurement is proportional to the stability of the modulation frequency, the instrument is recalibrated after each line is measured. The required agreement between the modulation frequency and the frequency of a quartz oscillator was 4:10<sup>8</sup>. It was estimated that the centering of instruments and phase comparison within the Geodolite cause an error of  $\pm 1$  mm, and an error in the average pressure, temperature and vapour pressure of .3 mb, .1°C, and 3 mb respectively cause an error of .1 ppm each. By staying in continuous radio contact with the pilot, the flight path was kept very close to the optical path. The airspeed was kept constant, and was accounted for when determining the average temperature.

To test the reproducibility of the data, the authors resurveyed a network of 30 lines. The surveys were done within a three month interval, so that tectonic movement did not affect their measurements critically, but there was a



good meteorological contrast. The differences in line lengths were plotted against the line length, and 77% and 93% of the points were found to lie between  $\pm\sigma_1$  and  $\pm 2\sigma_1$ , where  $\sigma_1$  ranges from 4mm and 10mm for lines 1km and 30km respectively.

The need for an aircraft makes these measurements extremely expensive, and measurements must be done during the daytime, as was pointed out by Slater and Huggett (1976). The repeatability of these measurements is usually not tested because of the expense. The lines measured ranged from 1 to 35 km with standard deviations given by the authors as 3 mm to 8 mm respectively.

In 1976, Slater and Huggett developed and tested a multiwavelength distance measuring instrument. This instrument uses a red He-Ne laser (632.9 nm) and a blue He-Cd laser (441.6 nm) along with a microwave source. The difference in measured path lengths for the two laser beams gives an atmospheric correction. Suppose the measured length is  $L+S$ , where  $L$  is the true length, and  $S$  is the extra length due to the atmosphere.  $S$  is therefore given by

$$S = \int_0^L (n-1) dl$$

and the difference in  $S$  obtained at two different wavelengths (red denoted by subscript one and blue by subscript two) is given by:

$$\Delta S = S_2 - S_1 = \int_0^L (n_2 - n_1) dl$$

$$= \int_0^L A_1 (n_1 - 1) dl \quad (1.1)$$

where  $A_1 = (n_2 - n_1) / (n_1 - 1)$  is only weakly dependent on atmospheric density and composition, so that we can replace it by its average value  $\bar{A}$ , and take it outside the integral sign (Bender and Owens, 1965). Therefore,  $\Delta S = \bar{A} S_1$ .  $\Delta S$  can be measured, and  $\bar{A}$  can be calculated from published values of the index of refraction for the two wavelengths, and a rough knowledge of the water vapor content. If  $\Delta S$  is known to  $\pm 3\%$ ,  $L$  can be calculated to 1 ppm or better. The uncertainty in water vapor pressure along the path gives an error of .1 ppm per millibar. The index of refraction is very sensitive to water vapor at microwave frequencies, therefore a third wavelength in the microwave range is added to the instrument to determine the average vapor pressure along the path. Precision of a few parts in  $10^6$ , for path lengths of up to 50 km and moderate temperatures, should be possible using this instrument. Field tests show excellent results up to distances of 10 km.

At distances greater than 10 km, ambiguity errors arise. In this instrument, the modulation frequency is adjusted such that any remaining fraction of the modulation wavelength is made zero. An error in the measurement of  $k$ , the number of whole wavelengths, was called ambiguity error by Slater. Using a single wavelength, the ambiguity error is resolved by slewing the modulation frequency from  $f_1$  to  $f_2$ .

The error in  $k$  is given by (see Slater, 1975):

$$\delta k = 2k \delta f / (f_2 - f_1) \quad (1.2)$$

where  $\delta f$  is the error in  $f$ . The electronic stability of their present EDM system can determine the frequency to an accuracy  $\delta f / (f_2 - f_1) \approx 5 \times 10^{-6}$ . Therefore ambiguity errors arise when  $k$  becomes greater than  $10^5$ , which corresponds to a range of about 10 km with a modulation frequency of 10 cm.

Another factor which limits the range in this instrument is the signal to noise ratio. To allow successful solution of the multi-wavelength distance equations, the signal to noise ratio needs to be high. This means that signal attenuation due to spreading and scattering plays an important role in a multi-wavelength instrument.

Tectonically interesting strains can be observed using small survey networks of aperture not exceeding 2 km (Margrave, 1980). In fact, small-aperture networks are preferred for measuring strain, to avoid averaging out significant strain variations (Savage and Prescott, 1973). In his study of the Peruvian Andes, Margrave used a Hewlett Packard 3800 EDM. This particular unit uses four different modulation frequencies of an infrared beam to give a reading to within  $\pm(5 \text{ mm} + 7 \text{ mm/km})$ , with a maximum range of 3 km. With a large number of repetitions of distance measurements, they were able to attain standard deviations comparable to those obtained by Savage et al. in California. Atmospheric

corrections were done only at the end points (at the instrument and at the reflector), and a linear relationship was assumed for all points in between. The instrument was calibrated before and after the field work, and the modulation frequency was found to be very stable.

### 1.1 EDM Accuracy

In the late summer of 1981, the HP3800 was tested and compared to a Sokkisha Red 1A EDM. The Sokkisha has a maximum range of only 2 kilometers, but is more compact, easier to use and can take readings at a rate of approximately once per 6 seconds. The manufacturer's specifications give the standard deviation as  $\pm(5 \text{ mm} + 5 \text{ mm/km})$ . The atmospheric correction is in steps of 10 ppm, whereas it is continuous on the HP3800. The Red 1A was tested in the continuous read-out mode, (figure 1) at approximately  $15^{\circ}\text{C}$  under very windy and dry conditions. The instrument was turned on at 2:40 pm, which corresponds to 0.00 seconds in the figure. Warm-up time seems to be about 100 seconds. The instrument was accidentally moved by almost 4 mm at 1400 seconds, while changing the battery. This would not happen had we used concrete pillars like those used in the microgeodetic network in Mexico (Nyland et al, in preparation). From 100 seconds to 1400 seconds, the standard deviation came to 2.5 mm, which is well within the manufacturer's specifications. and is comparable to

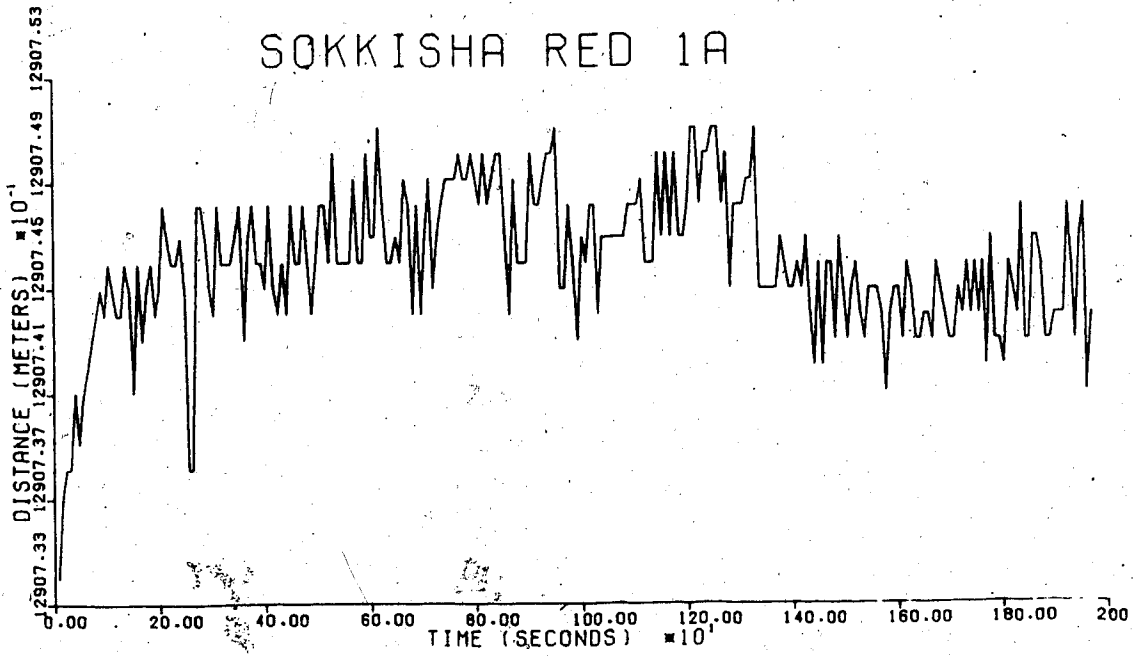


Figure 1.... Performance of the Sokkisha EDM under windy conditions. 0 seconds corresponds to 2:40 pm.

Margrave's deviations which range from 1.8 mm to 4.0 mm (Margrave, 1980, p56). In a comparison of the two EDM units (figure 2), the standard deviation was calculated using the formula given by Savage and Prescott (1973)

$$\sigma = (a^2 + b^2 L^2)^{.5} \quad (1.3 a)$$

where  $\sigma$  is the standard deviation for each instrument. The combined deviation of both instruments is therefore given by  $\sigma_2$ :

$$\sigma_2 = (2a^2 + 2b^2 L^2)^{.5} \quad (1.3 b)$$

For an ideal normal distribution, 68% and 95% of the points lie between  $\pm\sigma$  and  $\pm 2\sigma$  respectively, therefore we can take  $a=3$  mm and  $b=3 \times 10^{-6}$ . These values give 70% and 97% of the points between  $\pm\sigma$ , and  $\pm 2\sigma$ .

There seems to be a slight bias toward the positive, which means that the Sokkisha gave consistently higher values for the same distance than the HP3800. This was probably due to the instrument constant, which was later found to need slight adjustment. To test this, two reflectors were placed about 100 meters apart, with the instrument roughly half way between them and the distance to each reflector was measured and added to give the total distance. One of the reflectors was then replaced by the instrument, and the total distance was measured directly.

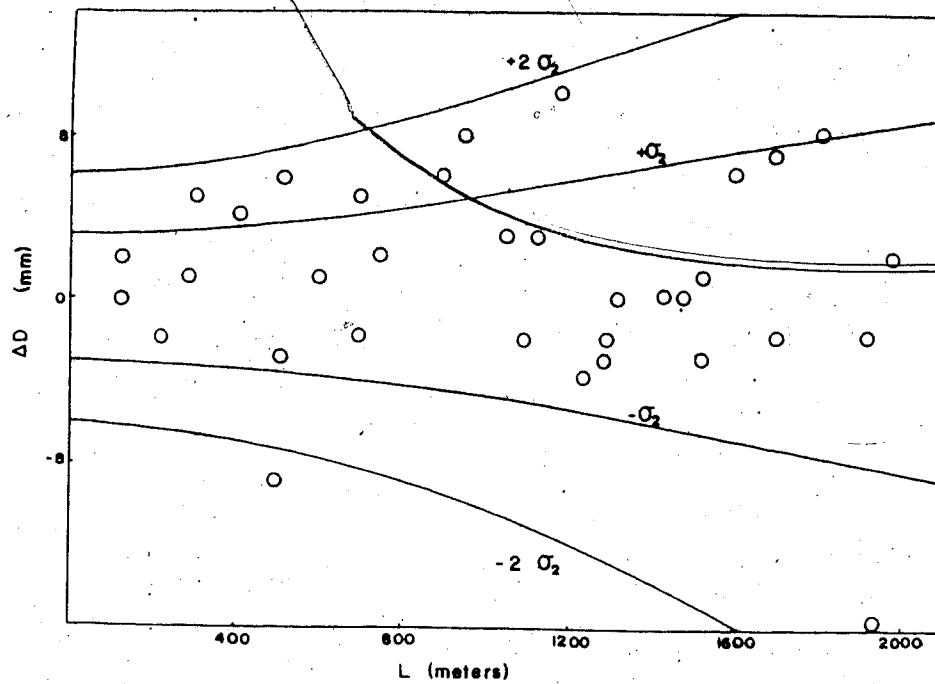


Figure 2.... Difference between distance measurements of the SOKKISHA and HP3800 infrared EDM units. 70% of the points lie between  $\pm\sigma_2$ ; 97% lie between  $\pm 2\sigma_2$ .

The difference between these two values is called the instrument constant.

Figures 3 and 4 show the percentage of return signal as a function of area of reflector surface (figure 3), and as a function of distance from the center of the reflector (figure 4). The maximum return signal is dependent on the distance of the instrument from the reflector, and on the weather conditions. From figure 4, the spreading of the beam can be calculated to be about  $10^{-3}$  radians. Due to the spreading of the infrared beam and the use of corner cube reflector, the pointing of the instrument at the reflector is not critical; a good reading can be taken with a return signal of 25% or more. The background level was about 15% in both cases (fig. 3 and 4); readings were taken under hot and windy weather conditions. The three corner cube reflectors (5 cm diameter each) were set up in a triangular configuration with the centers of the prisms separated by 6cm. The effective radius of the reflector was about 5 cm.

Even with stable monumentation, repeated surveys of geodetic networks are expensive and require a high commitment of manpower. Under normal circumstances, one should allow 2-3 weeks for a survey of a typical network (35-40 distances and approx. 80 angles) (Margrave, 1980).

I propose an alternative observation method. If the position of discrete points on the surface of the earth is recorded photographically at different times, a comparison of the two records by an optical Fourier technique might



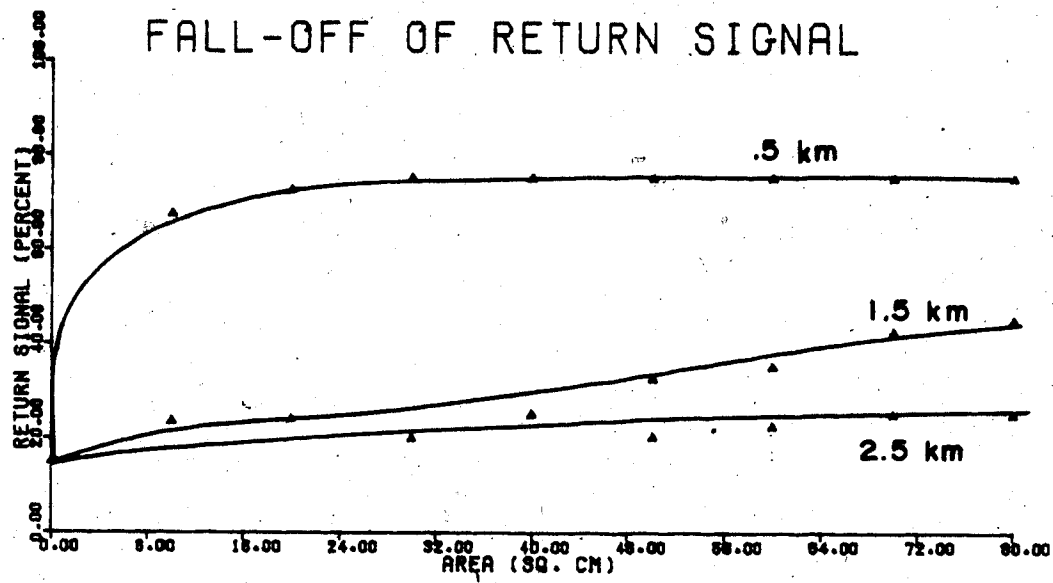


Figure 3.... Fall-off of return signal with decreasing reflector surface area for three different distances for the HP3800

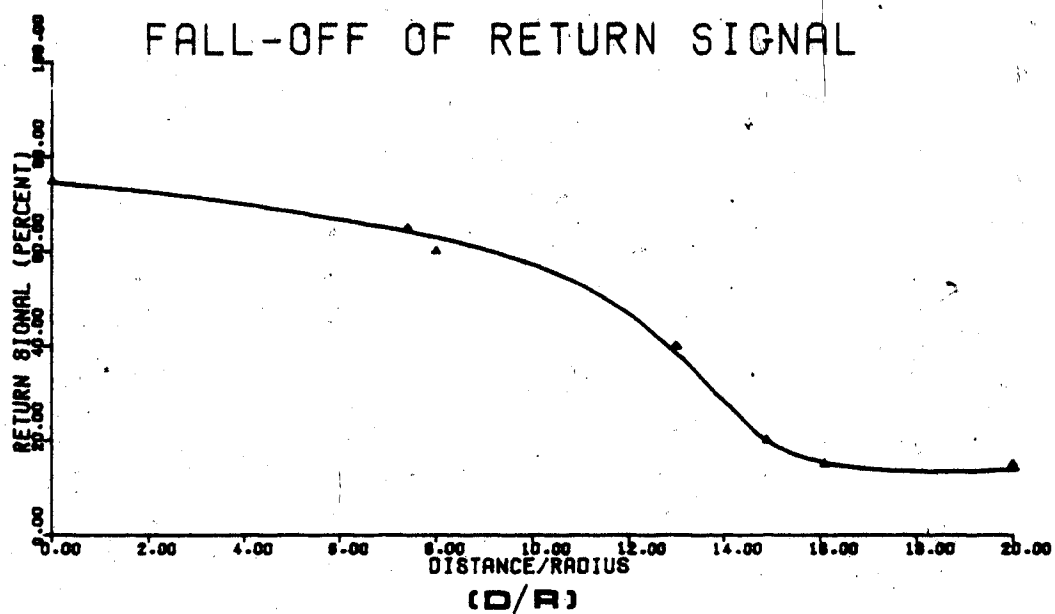


Figure 4.... The return signal reaching the instrument pointed a distance  $D$  away from the reflector of radius  $R$ , 1290 meters away. Spreading of the beam is therefore about .001 radians.

serve to determine the strain which has accumulated during that time.

One point on the ground will be taken as the reference point. Limitations on the precision of camera alignment will result in slight displacement of and rotation about this point. The method is thus capable of measuring accumulated strain, but not the actual displacements. The attainable accuracy is limited by the atmosphere, as in the previously discussed methods. Atmospheric conditions for desert areas, and measurements of atmospheric turbulence are discussed in detail by Walters and Kunkel (1981).

It is the aim of this work to find the theoretical feasibility of this method.

## 2. IMAGING SYSTEMS

To understand the approach we will take in analyzing our two photographs, we need to first look at imaging systems and how they work. In particular, we want to look at the part of imaging systems theory called frequency analysis of optical systems, or Fourier optics. In this, and all following chapters, 'frequency' is taken to mean the spatial frequency. When speaking about the light source, I will refer to its wavelength only, to avoid confusion. It is beyond the scope of this chapter to give more than a superficial treatment of Fourier optics; a number of good books are available on the subject. (eg, Goodman, 1968)

As an example, consider a simple imaging system, consisting of a point source, a camera and film. In the resultant photograph, the point will be spread by an amount determined by the resolution of the film and the size of the camera aperture. That is, both the camera and the film have a point spread function associated with them.

In any real camera, lens aberrations, and errors due to the camera frame cannot be made exactly zero. These aberrations can be minimized in a compound lens consisting entirely of spherical surface lenses, by use of elaborate computer programs which find optimum configurations, and appropriate multi-layer coatings. In good terrestrial cameras, the aberration errors are small, and some of these errors will cancel out when we compare two photographs taken with the same camera and lens, since we are only interested

in relative displacements.

## 2.1 Lenses

The most important components of optical systems are lenses. Consider a thin converging spherical lens (a lens is said to be thin if its radii of curvature are much greater than its thickness). A lens is made of material optically denser than air, and hence it will delay a light ray by an amount proportional to the thickness of the lens at that point. Assume we have a spherical lens of thickness  $T(x,y)$ , with a maximum thickness  $T_0$ . If  $g(x,y)$  is the complex amplitude distribution immediately in front of the lens, and  $g'(x,y)$  is the distribution immediately behind the lens, (figure 5) then

$$g' = t g \quad (2.1)$$

where  $t$  is the phase transformation and is given by:

$$t = \exp(ikT_0) \exp(ik(n-1)T(x,y)) \quad (2.2)$$

In this equation the term containing  $nT$  is due to the phase delay in the lens, and the term containing  $(T_0 - T)$  is due to the delay by the space adjacent to the lens.  $k$  is the wave number, given by  $k = 2\pi/\lambda$ .

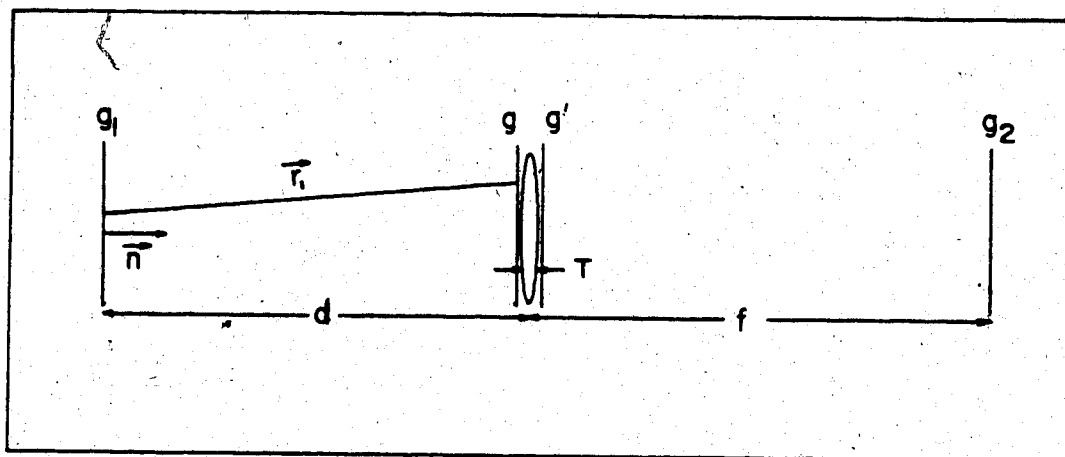


Figure 5.... Object with complex amplitude distribution  $g_1$  is placed in front of a convex thin spherical lens of focal length  $f$ . The resulting amplitude distribution is  $g_2$ .

From the geometry of a lens with spherical surfaces with radii of curvature  $R_1$  and  $R_2$ , we can calculate the thickness of the lens at any point  $(x, y)$ :

$$\begin{aligned} T &= T_0 - (x^2 + y^2) / 2 \left( \frac{1}{R_1} - \frac{1}{R_2} \right) \\ &= T_0 - (x^2 + y^2) / (2f(n-1)) \end{aligned} \quad (2.3)$$

where we used the lensmaker's formula in the last step. The phase transformation will therefore be (if we substitute (2.3) into (2.2) and drop the constant phase delay,  $\exp[iknT_0]$ ):

$$t = \exp[-ik(x^2 + y^2) / 2f] \quad (2.4)$$

The complex amplitude distribution behind the lens is therefore given by:

$$g'(x, y) = g(x, y) \exp[-ik(x^2 + y^2) / 2f] \quad (2.5)$$

One of the most useful properties of a converging lens is its ability to perform a two dimensional Fourier transform. The back focal plane of a converging lens contains the Fourier transform of a coherently illuminated object placed in the front focal plane (proof is given in the Appendix). The back focal plane is therefore called the transform plane, or frequency plane, and the front focal plane is usually referred to as the input plane.

In interferometry, we often talk about phase differences of a given number of wavelengths. Since fully monochromatic light is impossible to attain, we cannot have a path difference of one wavelength precisely for all the wavelengths in the beam. The degree of monochromaticity of the light is called temporal coherence.

Because mathematical point sources are excludable in principle, rays reach a point in an interference pattern from all points in the source "point". Perfect matching is therefore impossible. The degree of approximation of a source to a point source is called spatial coherence.

Before the invention of lasers, good coherence was achieved by spectral filtering and by making the source very small (resulting in considerable light loss). Lasers can only amplify photons if their wavelengths and directions of travel lie in certain narrow bands, and therefore good coherence is achieved without light loss.

The effects of coherence on imaging systems have been discussed by P. Consideine (1966), and will be summarized in the next section.

## 2.2 Effects of coherence on imaging systems

The highest frequency passed by a lens depends on its aperture. Suppose we are trying to image a sharp edge, (such as that of a razor blade) containing very high frequency components. A sketch of intensity versus distance



perpendicular to the edge was made (figure 6). An examination of a photograph of a coherently or incoherently illuminated edge will show this type of an intensity distribution. The same distribution can be derived theoretically (see Considine, 1966). From the sketch, two things are immediately apparent:

1. The coherent illumination produces ringing or intensity oscillations about  $I_0$  (the Fresnel diffraction of an edge).
2. On the basis that the edge is located at the half-intensity point, the coherently-illuminated edge is shifted. (see Considine, 1966)

The two effects are a result of the difference between transfer functions of coherent and incoherent imaging systems. That is, the transfer function of an optical system depends on the type of illumination. In the frequency plane, a coherently illuminated lens has a sharply cut-off transfer function, whereas the transfer function of an incoherently illuminated lens decreases gradually with frequency. If the cut-off frequency is lower than the highest frequency of the edge, ringing will occur in the coherent system. This is important, since ringing greatly influences the resolution. Considine shows that a lens which can resolve 114 lines/mm when incoherently illuminated, only resolves 36 lines/mm when a coherent light source is used, because the ringing of one line starts to overlap the next closest line.

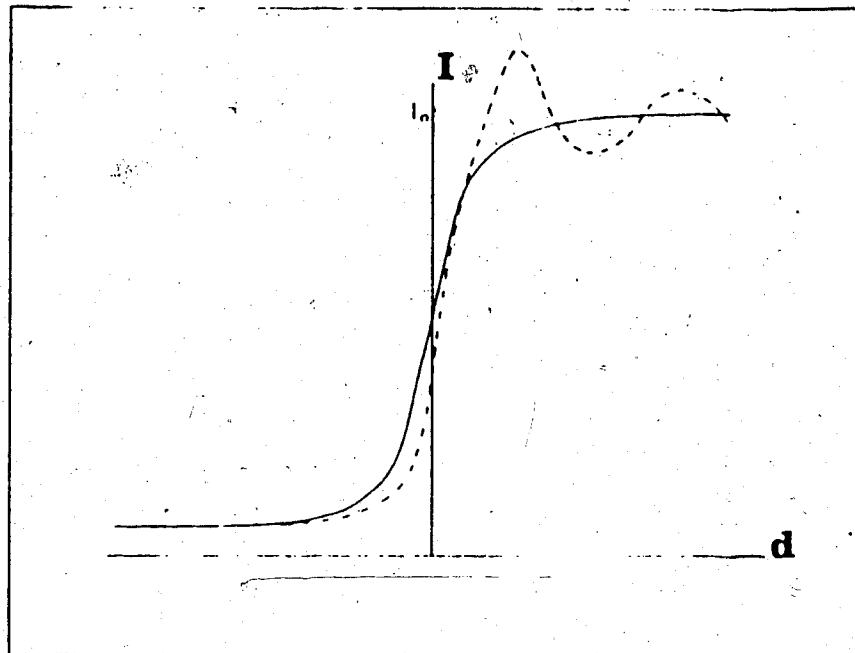


Figure 6.... Image of a sharp edge: Intensity as a function of distance perpendicular to the edge. Dashed line represents coherent illumination; solid line represents incoherent illumination of the edge

Another effect of coherent illumination is speckling, which is not a property of the light beam itself, but is present only when phase variations are introduced into the wavefront by transmission through an optically rough surface such as a scotch tape, or by reflection from a rough surface such as a painted wall. The size of the speckles depends on the wave number, and they can thus be made small enough to be useful in certain types of experiments (Khetan and Chiang, 1976) which will be discussed later.

There is no sign of edge ringing within the speckle pattern. A simple experiment can show that the absence of edge ringing is not caused by loss of coherence:

Passing a laser beam through a diffuser such as a scotch tape produces a speckle pattern. Placing a double slit in contact with the diffuser produces clear interference fringes across the speckle pattern. The field thus remained coherent after having been diffused.

### 2.3 Optical Processing

If  $g_1$  is the input function and  $g_2$  is the corresponding output for a linear system,

$$g_2(x', y') = \iint_{-\infty}^{\infty} g_1(x, y) p(x', y'; x, y) dx dy \quad (2.6)$$

where  $p$  is the impulse response, or the point spread function. If the system is space-invariant, then  $p$  depends

only on the distances  $(x'-x)$  and  $(y'-y)$ .

$$g_2(x', y') = \iint_{-\infty}^{\infty} g_1(x, y) p(x'-x, y'-y) dx dy \quad (2.7)$$

which is just the two dimensional convolution:

$$g_2 = g_1 * p \quad (2.8)$$

Taking the Fourier transform, we get:

$$G_2(u, v) = G_1(u, v) P(u, v) \quad (2.9)$$

where  $P$  is the Fourier transform of  $p$ , and is called the transfer function of the system.

Consider a plane wave illuminating an input placed at plane  $P_1$ . (figure 7) A thin spherical lens  $L_1$  is placed a distance  $f_1$  from  $P_1$ , where  $f_1$  is the focal length of the lens. In the back focal plane of the lens will appear the Fourier transform of the object. This plane is called the transform plane, and is denoted by  $P_2$ . We can Fourier transform this plane by the use of another lens. The output will appear in plane  $P_3$ , the image plane. The image is inverted, because we are performing two consecutive transforms, rather than a Fourier transform followed by an inverse transform. We therefore choose the coordinates in  $P_3$  in reversed directions, as denoted by the negative sign in figure 7. The magnification is given by the ratio of the

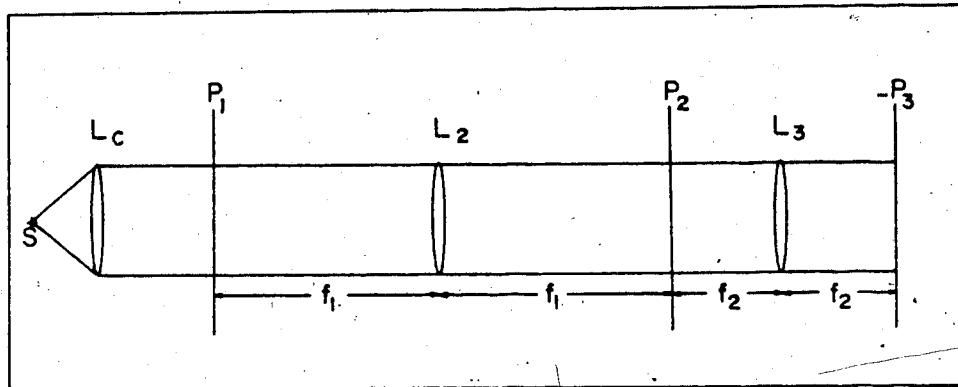


Figure 7.... Arrangement of an optical Fourier analyser

focal lengths of the two lenses, and is usually chosen to be unity. The plane  $P_2$  contains the Fourier transform of the input, with the spatial frequencies related to the spatial coordinates by:

$$x_2 = f\lambda u$$

(2.10)

$$y_2 = f\lambda v$$

By placing appropriate filters in the transform plane, we can therefore alter the image in the output plane. For example, to block out high frequency components of the input, we would place a small aperture at the transform plane. The highest frequency passed by a given aperture is given by equations 2.10.

The first attempts to manipulate the Fourier spectrum of an image were done in 1893 by Abbe, and a few years later by Porter. The Abbe-Porter experiments are a good demonstration of the principle of Fourier analysis. A fine wire mesh is placed in a collimated coherent beam, in the front focal plane of a lens. The back focal plane will contain a rectangular array of dots, the Fourier transform of the mesh. With a narrow horizontal slit, passing only one row of spectral components, the image will contain only the vertical components of the wire mesh input.

Most useful filters are harder to fabricate, and until the development of digital-optical converters, they could only be approximated. These filters are used to attenuate

undesired effects such as linear smear, blur or atmospheric effects in photographs. It is hoped that the transfer function of the compensating filter will remove the transfer function of the undesired effect, therefore the filter is given by (if we ignore noise):

$$F(\vec{v}) = 1 / P(\vec{v}) \quad (2.11)$$

where  $P(\vec{v})$  is the Fourier transform of the point spread function of the effect we want to remove. For example, the point spread for linear smear is a rectangle function, and the transfer function is simply its Fourier transform, which is the Sinc function.

If additive noise is present, however, the filter given by equation 2.11 could degrade the photograph instead of improving it, depending on the signal to noise ratio. To include the noise, we start with the equation for a linear system (eqn. 2.6). In this example, our system consists of an object, atmosphere, a camera and film. The output  $o(x',y')$  is related to the input  $i(x,y)$  by

$$o(x',y') = \iint_{-\infty}^{\infty} i(x,y)p(x'-x,y'-y)dx dy \quad (2.12 a)$$

$$O(u,v) = I(u,v)P(u,v) \quad (2.12 b)$$

$P$  contains all lens aberrations and conditions which may degrade the image. The overall transfer function is

therefore given by:

$$P = P_A P_L P_M P_r \quad (2.13)$$

where:

$P_A$  = atmospheric transfer function,

$P_L$  = transfer function of the lens

$P_M$  = transfer function of motion during exposure

$P_r$  = transfer function due to the film.

We now complete the model by considering noise. The noise, which we will assume to be additive, consists of all the random processes present, such as dirt, dust, discontinuities, film grain and laser speckle. The observed image is therefore

$$o(x,y) = i(x,y) * p(x,y) + n(x,y) \quad (2.14)$$

If we take  $\hat{i}(x,y)$  to be the estimate of  $i(x,y)$ , then the error function  $e(x,y)$  is just  $\hat{i}(x,y) - i(x,y)$ , and has the power spectrum  $|E(u,v)|^2$ . The mean square error will be given by:

$$MSE = \iint_{-\infty}^{\infty} W(u,v) |E(u,v)|^2 du dv$$

where  $W$  is a frequency weighting function. For example, for frequencies which we consider unimportant, we can put  $W$  equal to zero.



If we assume that the noise is not correlated with the signal, then for a linear system, minimizing the mean square error gives (see Considine and Gonsalves, 1978):

$$F(\vec{\nu}) = \frac{1}{P(\vec{\nu})} \frac{\left| \frac{O(\vec{\nu})}{N(\vec{\nu})} \right|}{\left| \frac{O(\vec{\nu})}{N(\vec{\nu})} \right|^2 + \left| P(\vec{\nu}) \right|^{-2}} \quad (2.15)$$

which is known as the Wiener filter. It was first designed to improve atmosphere-degraded images. The estimate of the input,  $\hat{I}$  is  $O(u,v) \cdot F(u,v)$ . It can be seen that if the signal to noise ratio is very large, this reduces to the inverse filter,  $1/P$ . Thus for a system with infinite signal to noise ratio, we get:

$$\hat{I} = OF = IP/P = I \quad (2.16)$$

#### 2.4 Atmosphere

In this section, we assume that in our system, there is no limitation on size or quality of the lens, or resolution of the film. The light beam we are recording will be distorted by inhomogeneities in the refractive index of the atmosphere through which it travels. D.L. Fried (1966) calculated the effects of the atmosphere on a point source as a function of altitude, using a model of vertical

distribution of the index of refraction structure parameter,  $C_N^2$  based on experimental data. He found that at an altitude  $h$ ,

$$C_N^2 = 4.2 \cdot 10^{-14} h^{-1/3} \exp(-h/h_0) \quad (2.17)$$

where  $h_0$  was found to be 3200 m.  $C_N^2$  is a coefficient which measures the strength of the refractive index turbulence, a function of both time and space. It is usual to measure the temperature structure parameter  $C_T^2$ , which is directly proportional to  $C_N^2$ . Another parameter which is often used to give a measure of turbulence is the transverse coherence length,  $r_0$ . The relation between  $C_N^2$  and  $r_0$  is:

$$r_0 \propto \left[ \int_0^L C_N^2(z) dz \right]^{-3/5} \quad (2.18)$$

For a long exposure, the maximum resolution  $R$  has been defined as the limiting value of the resolution  $R$ , as the diameter of the lens becomes infinitely large. In terms of the altitude  $z$ , Fried gets:

$$R = (\pi/4) (r_0 / \lambda z)^2 \quad (\text{cycles/meter})^2 \quad (2.19)$$

At an altitude  $z$ , there is a minimum size of an object which we can see. The maximum spatial frequency is given by the square root of the resolution, and is in units of line pairs per meter. The minimum resolvable length is :

$$I = 1 / 2(R)^2 \quad (2.20)$$

R approaches its limiting value asymptotically as the lens diameter D becomes very large. When  $D=2r_0$ , R is almost 70% of  $R_0$ . When D equals  $r_0$ , R is approximately  $.45R_0$ .

The transverse coherence length  $r_0$  has been measured accurately for mountain and desert areas by Walters & Kunkel (1981). During the night,  $r_0$  in the desert is fairly constant until sunrise, with a mean value of 50mm. Optical turbulence is lowest ( $r_0$  is at a maximum) when the temperature of the ground is equal to the temperature of the air. This occurs just after sunrise, and just before sunset.

## 2.5 Optical monitoring of surface deformations

The method proposed here is a variation of the idea of Vacquier and Whiteman (1973), who used a camera of 10-meter focal length to photograph two pairs of lights, one on each side of an active fault. Average displacement over the past 5 million years on this portion of the fault is 6 cm/year. The separations of the dots on the photographic plates were measured using a 10-power microscope with a micrometer screw. If there is a horizontal temperature gradient, a systematic error would be introduced. This error would be canceled out by another camera, pointed in the opposite direction. This second station was never built, mainly because of the expense, and because the authors felt that it

would not significantly improve the precision.

Over a two year period, the expected 12 cm displacement was not observed. The authors believe this is because the fault is locked, and over the distance of 25 km (the distance between the camera and the far pair of lights) the strain is linear. Since they were measuring parallax, only a non-linear strain could be detected.

Even though their experiment did not give the expected results, much can still be learned from their data (p 862, JGR, vol.78, no.5). There is a great variation in the quality of the photographs. The size of the spots can vary from .15 to .5 mm. The photographs were taken in twenty minute intervals, in which the size of the spots could change by a factor of 2 or more.

Two pairs of dots appear on each photograph: the inner pair being the image of the far lights (25 km), and the outer pair the near lights (8 km). The inner pair may appear above or below the outer pair, depending on the vertical temperature gradient during the exposure. The vertical displacement of the inner dots varies from about .2 mm to -.1 mm. Horizontal temperature gradient cannot be observed from these photographs.

The expected shift of the inner pair of spots is .05 mm over the two year period. Averaging over a large number of photographs, the authors claim to be able to detect a shift of .002 mm (corresponding to a ground movement along the fault of 4 mm).

Our method will differ in two ways. One, we will use a random array of light sources or reflectors; and two, we will process the data using a double exposure interferometric technique. The area of study (approximately 1 square kilometer) will be an active fault in a desert area in northern Mexico (Darby et al., 1981). The motion along the fault is almost entirely horizontal, and expected maximum yearly displacements are 1 to 2 cm. An array of precisely positioned reflectors in the area will be imaged on a 10 by 10 cm high resolution film, on an Estar base or glass plate for good stability. Holographic films with a resolution of 500 to 2000 lines/mm are commercially available on long lasting stable bases. For more discussion on recording media, see Goodman (1968).

The recording of the lights is thus the same as the Vacquier and Whiteman experiment on a smaller scale. Where their line of sight was 25 km, ours will be about 1 km. Their 10 meter focal length lens has a resolution of approximately 25 microns, and the displacement they were looking for was 50 microns. Our lens will have a focal length 5 to 10 cm, with a resolution .5 to 1 micron, and the displacement we are looking for is 1 to 2 microns. Our system will be manually operated whereas theirs was automatic, but Vacquier and Whiteman ran into some problems with their automatic system, and most of their useful data was taken manually. Photographs should be taken approximately every twenty minutes, because atmospheric

conditions can change significantly in this time interval, and the size of the images of the reflectors will vary. When we compare two transparencies separated in time by one or two years, we will choose the two in which the size of the reflector images is similar.

It is assumed that an area 10 meters in length will have a uniform displacement rate, and that it is sufficient to use an array of reflectors with a separation of about 10 meters. The transparencies will be compared using a double exposure interferometry technique. The attainable accuracy will be discussed in chapter 4.

The position of the reflectors is not critical, but a line perpendicular to the fault and passing through a point directly beneath the camera (referred to as the main axis from now on) will have the least error, since the vertical index of refraction gradient only affects precision on the component perpendicular to the fault. The reflectors should therefore be concentrated near the main axis, as shown in the lower part of figure 8. (Black squares represent reflectors). When in the field, it is usually impossible to make a straight row of lights which does not deviate from the main axis. It is therefore useful to estimate the error introduced by the vertical refraction gradient. A camera on top of a mountain at a height  $h$ , is pointed at point  $P$  below (where  $P$  is the position of the reflector which deviates most from the main axis). The light rays will follow a bent path, and the image of  $P$  will seem to originate at  $P'$

(figure 8).

The ground in a desert area at night cools off very rapidly. Dense air near the ground is cooled, and thus tries to maintain its position near the ground. Thus atmospheric turbulence is near minimum during the desert night. A detailed discussion on measurements of atmospheric turbulence in a desert area can be found in a paper by Walters and Kunkel (1981).

The assumption I make is that the index of refraction varies linearly with altitude  $z$ . That is,  $n(z)=c+kz$ . From Snell's law we have that  $n(z)\sin\theta(z)$  is a constant. The distance  $s$  is thus given by:

$$s = \int_0^h dz \tan\theta(z)$$

$$= (a/k) [\cosh^{-1}((c+kh)/a) - \cosh^{-1}(c/a)] \quad (2.21)$$

where  $a = \sin\psi$ , and  $\theta$  is the angle at any point along the curved path to the vertical. As a specific example, suppose the vertical temperature gradient is 5 degrees per 100 meters, of altitude. This value is extremely high; in most cases, the gradient will be much less. Since a change of  $1^\circ\text{C}$  causes a change in the refractive index of  $\Delta n/n = 10^{-6}$ . This gives  $k = 5 \times 10^{-5} \text{ km}^{-1}$ . For  $\psi = 60^\circ$ , and  $h = .5 \text{ km}$ , the error in the position of the reflector will have a component parallel to the fault equal to  $10^{-4}y$ . For  $y = 100 \text{ meters}$ , this is 1 cm. This error will be reduced by about one order of magnitude

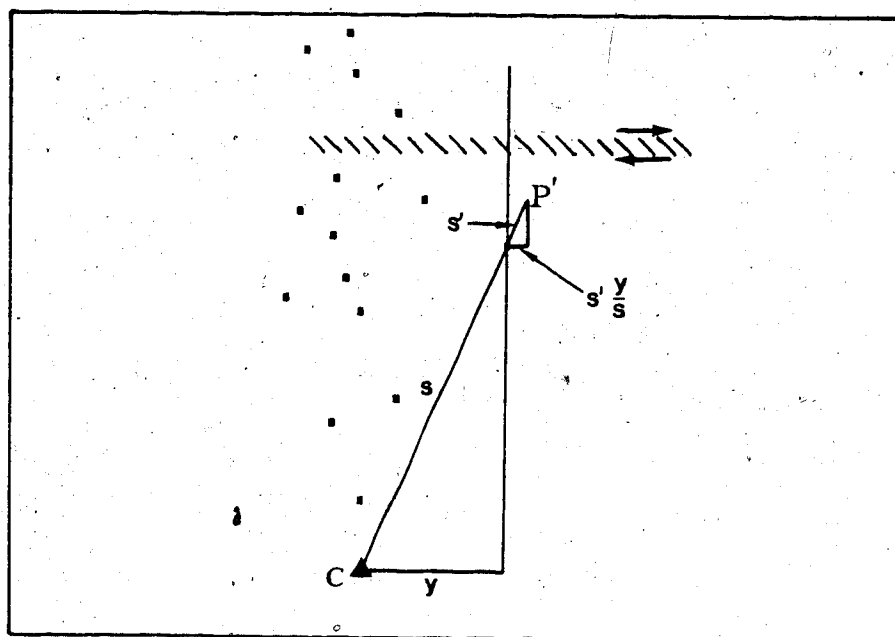
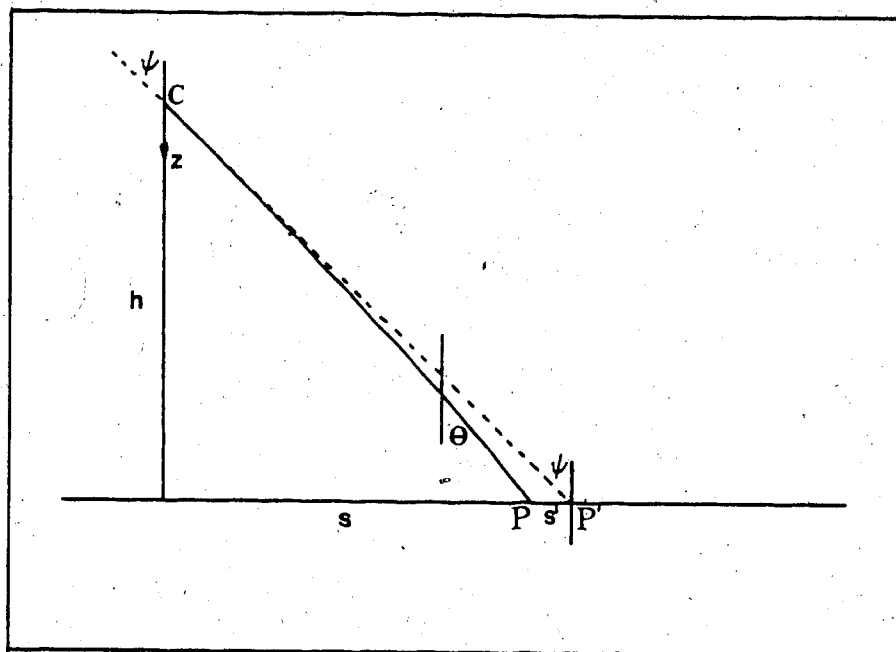


Figure 8.... Above: side view of the path followed by the rays from point P to the camera at C. Below: top view - distance  $s$  split up into its components parallel and perpendicular to the fault.



if the vertical gradient of  $n$  is approximately the same during the exposure of the second photograph.

A horizontal temperature gradient, if one occurs, will be much smaller than the vertical gradient. A horizontal gradient of  $2^\circ/\text{km}$  for example, at  $45^\circ$  to the line of sight would cause an error of 1 mm in the position of a point about 1 km from the camera. It was found by Vacquier and Whiteman, (1973) that this error due to horizontal gradient was too small to affect their results significantly. Since our lines of sight are much shorter than theirs, we can neglect the error due to horizontal refractive index gradient.

It is obvious that the camera cannot be positioned so precisely that each light would be exactly aligned, (were there no movement along the fault at all) and it is also unlikely that the average refractive index will be the same at the time the second photograph is taken. Thus there will be a small displacement between the lights as seen on the photographs. In chapter 4, it will be shown that it is not only preferable, but necessary to add a displacement (not necessarily a known displacement) before the comparison can be made. Because of this unknown added displacement, only non-uniform strains can be detected. The results of chapter 4 also show that high frequency noise does not present a serious problem. To get the yearly strain rate, a comparison of two photographic records, separated in time by one year, will be made.

A method capable of detecting such small differences in two transparencies will be discussed in chapter three.

several assumptions are made:

1. The same lens and same camera were used both times.
2. The lens was not damaged in between the two trials.
3. The transparencies and their transforms were stored carefully.
4. The experiment was carried out under conditions of minimum optical turbulence and under conditions of similar temperature and pressure.
5. Haze was removed by the use of colour filters.

A photograph contains a vast amount of data, and digitizing it would require exorbitant storage space. In our case however, the photograph is used to record the precise position of one or two hundred small points, with the rest of the photograph being dark background. Optical-digital converters have reached a high degree of sophistication; transparencies can be digitized with precision to 500 lines/mm. The experiment could therefore be equally well carried out digitally or optically. (as will be shown with synthetic data in chapter 4)

## 2.6 Preliminary Calculations

Using equation 2.13, and the results of the previous sections, it is possible to calculate the width of the intensity peaks on the transparency. It will be shown in

chapter 3 that the size of the image points ultimately limits the resolution of the interferometer. Assume the size of the transparency is a square decimeter, and the ground surface covers a square kilometer.

The following calculations are based on parameters of a commercially available terrestrial camera (Zeiss (Jena) UMK 10/1318). The compound aberration-corrected lens, camera frame and the film plate produce a combined error no greater than .008mm. For our purposes, this is not a negligible error, however using the same lens and camera will eliminate most of this error.

1. Resolution of film will be 1000 lines/mm , or  $10^5$  lines/dm. This corresponds to an object on the ground of diameter  $10^{-5}$ km, or 1cm. This is the minimum size of an object on the ground which we can resolve.
2. Using concrete pillars, it is hoped that the camera will not move during exposure, therefore the motion transfer function ( $P_M$ ) equals one, even for long exposure times.
3. The lens will have a radius of 2.5 cm and a focal length of about 50 mm. Using equation 2.10, the highest spatial frequency ( $u$ ) passed by the lens is approximately  $1/2\lambda$ . Taking the average wavelength of the source to be 500nm, we get  $u \approx 10^6$  lines/meter. This corresponds to an object on the ground with a diameter of 1cm. Smaller objects will not be passed by the lens. (The smallest object passed by a 100 mm lens of same dimensions would be 2 cm).

4. For  $D \approx r_0 \approx 5\text{cm}$ , we have (using equation 2.20),

$$R = .45R_0 = 3500 \text{ (cycles/m)}^2 \text{ ( for } z=1\text{km ) ,}$$

therefore  $l = .01\text{m} = 1\text{cm}$ .

These calculations pertain to long exposures (greater than one second). Long exposures average out very short variations in the index of refraction due to turbulence. Using long exposures does not make it unnecessary however to take as many photographs as one can.

5. Since we are taking an oblique photograph, some points will be farther than others, and thus some points will not be in perfect focus. The amount by which a point on the ground is spread will depend on the height of the camera and the position of the point. Assuming the points near the central line are in good focus, the nearest and farthest points will be spread by one to three cm.

The combined effect will be that a 10 cm source will be imaged onto an area of film larger than .01 mm, but not exceeding .02 mm. The above errors affect the size of the image points, but not their position. The following errors will alter the position of the reflectors.

1. The camera should be positioned such that any point which has experienced no movement will appear in the same position to within about 40cm. Suppose the camera is .3km above the area to be imaged, and 1km away from it horizontally, then the precision to which the camera must be positioned is  $7 \cdot 10^{-5}$  radians (vertically), and

$4 \times 10^{-4}$  radians (horizontally).

2. The horizontal gradient of  $n$  can introduce an error of about 1 mm in the position of the reflectors. A vertical gradient produces an error in the displacement along the fault which is proportional to the distance of the point from the main axis. This error will be of the order of 1 mm for points lying within 100 m of the main axis.
3. Distortions in the size or shape of the photographic plate due to temperature or humidity can cause errors in the position of all points in the image. If we require that this error be less than .1 micron, (ground displacement error of less than 1 mm) and we are measuring the distance between two points which are approximately .04 mm apart, then the plate distortion must be kept to less than .25%. We can impose a stronger condition on the distortion. If we examine each pair of dots by a laser beam of 1 mm diameter, and we require that all points illuminated by the beam have a position error of .1 micron, then the distortion must be less than .01%.

It is clearly demonstrated by the two photographs on pages 192 and 193 of Hecht and Zajac (1976), that today's cameras are capable of attaining the needed accuracy. The photograph was taken by a Hyac I panoramic camera with a 300mm f/5 lens (lens diameter=6cm). It covers an area of 3 by 6 km, and objects 30 by 60 cm can be clearly seen in the blow-up (second photograph).

### 3. INTERFEROMETRIC COMPARISON OF TRANSPARENCIES

Using a film with resolution of 1000 lines/mm enables us to record separations of  $10^{-3}$ mm.

Each of our two photographs will contain light peaks on a dark background. When superimposed on a single transparency by a double exposure, the new transparency or plate will contain pairs of peaks, separated by a small distance  $d$ . Due to the fact that the camera cannot be aligned exactly, and that the average index of refraction was slightly different when the first photograph was taken and during the exposure of the second photograph,  $d$  will not be entirely due to the strain accumulation on the ground surface. It is hoped that  $d$  will not be more than .06 mm, which is about three times the width of the peaks, because this will limit the the accuracy of the system (chapter 4).

Assume that the photographic plate has a resolution of 1000 lines (or picture elements) per millimeter, and that it has been properly exposed and developed. In pointwise filtering, we use a laser beam as a probe to examine a small portion of the photograph of diameter about 1 mm, which corresponds to 10 meters of the ground surface and thus contains only one reflector. In whole-field filtering, we examine the whole photograph at once, but we look at only one component of the displacement. Both methods will be discussed in detail later.

From now on, the units I will use will be picture elements. The conversion factor is given by the film

resolution. In our case, 1000 picture elements equals one millimeter. The diameter of the peaks thus becomes  $b=20$ , their separation will be 40 to 60, and the laser beam covers an area of diameter about 1000.

Our method for determining the displacement will be similar to the experiment of Khetan and Chiang (1976), and Chiang and Juang (1976), in which the authors used laser speckles to analyse strain on a plane surface under load. The random pattern formed by the speckles is a result of interference of coherent light bouncing off different parts of an optically rough surface. The pattern is recorded on high resolution film before and after the surface has been deformed by an applied load, by double exposure of the photographic film or plate. The double exposure is then Fourier transformed, to analyse the recorded strain information. The film contains pairs of dots, separated by a small distance  $d$ , one corresponding to the first exposure, and the other to the second. If we consider a section of the film which consists of only one pair of dots, the transmittance of that section approximates a pair of pinholes. The interference pattern produced by this section will therefore be a light circle modulated by parallel, equidistant fringes. The fringe separation will depend on the separation and relative orientation of the two pinholes.

Now, if we examine the whole film, the fringes produced by other pairs will have different spacing and orientation, and, therefore no clear pattern will be visible.

This problem can be overcome by two methods: Pointwise filtering, or whole field filtering. In pointwise filtering, we examine an area of the film which is small enough that the displacement in that section is uniform. We can do this simply by passing a laser beam (1 to 2 mm diameter) through the film, and observing the diffraction pattern on a screen. In the whole field method, we examine the whole film at once, and we place a small aperture in the frequency plane. We use another lens to perform the Fourier transform of the frequency plane. The output plane will then contain fringes which are the loci of points of equal displacement component. By placing an aperture at different positions  $(r, \theta)$  in the frequency plane, the fringes in the output plane change accordingly.  $r$  changes the spacing of the fringes, while  $\theta$  changes the component of displacement we are looking at. Thus the strain on the test surface can be calculated, however it is useful to know a priori if the deformation was in or out of the plane of the surface.

Our problem is identical to this, except that our pattern of dots is not completely random, and in our case, the pattern of dots is produced by reflectors positioned on the ground, rather than a speckle pattern produced by reflection of coherent light from a rough surface.

In the next sections, it will be shown mathematically that these fringes are a cosine<sup>2</sup> modulation of the light intensity in the frequency plane of a single exposure. The limitations which exist on the size of the spots will also



be given.

### 3.1 Recording a random pattern

In a double exposure method, we expose each of our two photographs on a single plate, one at a time.

Consider the complex amplitude of light  $h(x, y)$  in the object transparency (the first photograph) at the point  $P(x, y)$ . The light amplitude at  $P'$  due to radiation from  $P$  (figure 9) is given by the Huygens-Fresnel principle:

$$h(\exp(ikS))/i\lambda S \quad (3.1)$$

The total amplitude at  $P'$  is therefore:

$$\iint_{-\infty}^{\infty} [h(x, y)/i\lambda S] \exp(ikS) dx, dy, \quad (3.2)$$

The amplitude  $g(x_3, y_3)$  at point  $Q$  in the image plane is:  
(see Appendix)

$$g(x_3, y_3) = \iint_{-\infty}^{\infty} \left[ \iint_{-\infty}^{\infty} (h(x, y)/i\lambda S) \exp(ikS) dx, dy, \right] A(x, y) \cdot \exp[-ik(x^2+y^2)/2f] (\exp(ikS')/i\lambda S') dx dy \quad (3.3)$$

where  $A$  is the aperture function and  $f$  is the focal length of the lens.

$$S_3^2 = p^2 + (x_3 - x)^2 + (y_3 - y)^2$$

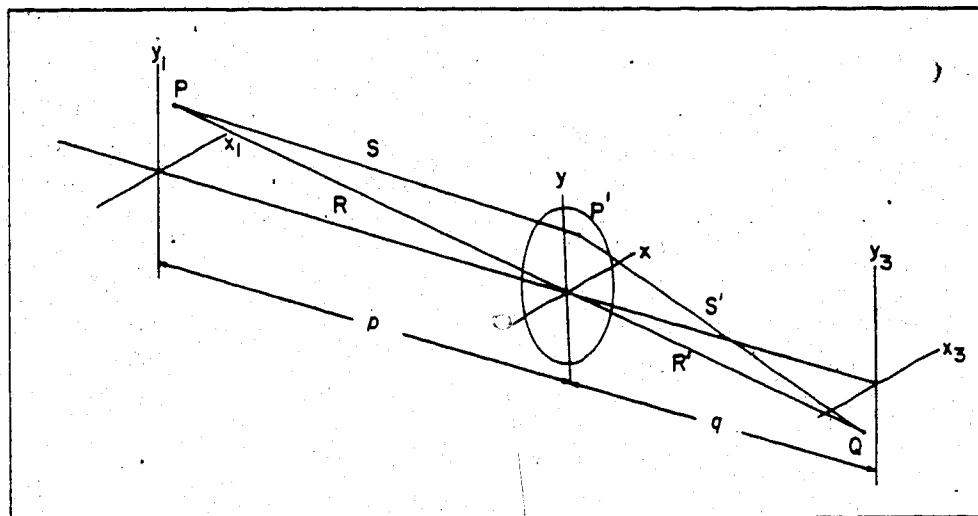


Figure 9.... Recording a random pattern

$$\begin{aligned}
&= p^2 + x^2 + y^2 - 2(x, x+y, y) + x^2 + y^2 \\
&= R^2 - 2(x, x+y, y) + x^2 + y^2 \\
S &\approx R - (x, x+y, y)/R + (x^2 + y^2)/2R \\
&\approx p - (x, x+y, y)/p + (x^2 + y^2)/2p \quad (3.4)
\end{aligned}$$

similarly

$$S' \approx q - (xx, +yy, )/q + (x^2 + y^2)/2q \quad (3.5)$$

These approximations apply when the planes  $P_1$  and  $P_2$  are far from the lens, and are known as the Fraunhofer approximations.

Assume the variations in  $S$  and  $S'$  are small, then  $S \approx p$  and  $S' \approx q$  can be considered constant (see Khetan and Chiang, 1976).

$$\begin{aligned}
g(x_2, y_2) &= (-1/\lambda^2 pq) \iiint h(x_1, y_1) A(x, y) \exp[-ik(x^2 + y^2)/2f] \\
&\quad \exp(ikS) \exp(ikS') dx_1 dy_1 dx_2 dy_2 \quad (3.6)
\end{aligned}$$

Now plug in equations (3.4) and (3.5)

$$\begin{aligned}
g(x_2, y_2) &= (-1/\lambda^2 pq) \iiint h(x_1, y_1) A(x, y) \exp[-ik(x^2 + y^2)/2f] \\
&\quad \bullet \exp[ik(p+q - (xx_1, +yy_1, )/p - (xx_2, +yy_2, )/q \\
&\quad + (x^2 + y^2)/2p + (x^2 + y^2)/2q)] dx_1 dy_1 dx_2 dy_2 \quad (3.7)
\end{aligned}$$

$$\begin{aligned}
&= -(\exp[ik(p+q)])/\lambda^2 pq \iiint h(x_1, y_1) A(x, y) \\
&\quad \bullet \exp[(ik/2)(x^2 + y^2)(-1/f + 1/p + 1/q)] \\
&\quad \bullet \exp[-ik((xx_1, +yy_1, )/p + (xx_2, +yy_2, )/q)] dx_1 dy_1 dx_2 dy_2 \quad (3.8)
\end{aligned}$$

but

$$1/f - 1/p - 1/q = 0 \quad (3.9)$$

therefore,

$$g(x, y) = K \iiint h(x, y) A(x, y)$$

$$\bullet \exp[-ik(x(x/p + x_0/q) + y(y/p + y_0/q))] dx dy dx dy \quad (3.10)$$

where

$$K = -(\exp[ik(p+q)]) / \lambda^2 pq$$

Double exposure is made with displacement (as observed in the image plane) being  $d(d_x, d_y)$ . Assuming the source shape does not change drastically with time, the total exposure at the image plane is:

$$e(x, y) = t[|g(x, y)|^2 + |g(x+d_x, y+d_y)|^2] \quad (3.11)$$

where  $t$  is the exposure time. Examples in chapter 4 show that small shape changes do not affect the results very much. We assume the film was properly developed; then the amplitude transmission function  $g'$  will be a linear function of exposure time, and

$$g'(x, y) = b - ce(x, y) \quad (3.12)$$

The amplitude of light behind the photographic record is:

$$g'(x, y) = b - ct[|g(x, y)|^2 + |g(x+d_x, y+d_y)|^2] \quad (3.13)$$

### 3.2 Whole field filtering

To obtain the displacement information from this pattern, we perform an optical Fourier transform in the usual way. We put the transparency in the input plane, so that  $g(x_1, y_1)$  in the previous section now becomes  $g(x, y)$ . The light intensity distribution at the transform plane of the lens is then the square of the Fourier transform of the amplitude transmission function  $g'$ .

$$I(x_2, y_2) = \left| \iint g'(x, y) \exp[-ik(x, x_2 + y, y_2)/f] dx, dy \right|^2 \quad (3.14 a)$$

Neglecting the constant (or DC) term  $b$ , which will give a bright spot at the center of the frequency plane, we get (away from the center):

$$I(x_2, y_2) = c^2 t^2 \left| \iint |g(x, y)|^2 \exp[-ik(x, x_2 + y, y_2)/f] dx, dy + \iint |g(x, +d_x, y, +d_y)|^2 \exp[-ik(x, x_2 + y, y_2)/f] dx, dy \right|^2 \quad (3.15)$$

From the shift theorem of a Fourier transform (see Appendix for proof), we get:

$$I(x_2, y_2) = c^2 t^2 \left| \iint |g(x, y)|^2 \exp[-ik(x, x_2 + y, y_2)/f] dx, dy + \left\{ \iint |g(x, y)|^2 \exp[-ik(x, x_2 + y, y_2)/f] dx, dy \right\} \cdot \exp[-ik(d_x x_2 + d_y y_2)/f] \right|^2 \quad (3.16)$$

therefore

$$\begin{aligned}
I(x_2, y_2) &= c^2 t^2 \left| \iint_{-\infty}^{\infty} |g(x_1, y_1)|^2 \exp[-ik(x_2 - x_1 + y_2 - y_1)/f] dx_1 dy_1 \right. \\
&\quad \cdot \left. \left\{ 1 + \exp[-ik(d_x x_2 + d_y y_2)/f] \right\} \right|^2 \\
&= I_1(x_2, y_2) \left| 1 + \exp[-ik(d_x x_2 + d_y y_2)/f] \right|^2 \quad (3.17)
\end{aligned}$$

where

$$\begin{aligned}
I_1(x_2, y_2) &= c^2 t^2 \left| \iint_{-\infty}^{\infty} |g(x_1, y_1)|^2 \exp[-ik(x_2 - x_1 + y_2 - y_1)/f] dx_1 dy_1 \right|^2 \\
\left| 1 + \exp(-iz) \right|^2 &= [1 + \exp(-iz)][1 + \exp(iz)] \\
&= 1 + \exp(-iz) + \exp(iz) + 1 \\
&= 2 + 2 \cos z \\
&= 2(2 \cos^2(z/2) - 1 + 1) \\
&= 4 \cos^2(z/2)
\end{aligned}$$

therefore

$$I(x_2, y_2) = 4 I_1(x_2, y_2) \cos^2[(k/2f)(d_x x_2 + d_y y_2)] \quad (3.18 a)$$

where  $I_1$  is the intensity distribution at the transform plane if only one exposure is recorded on the film. Most of the energy from this term is concentrated near the center of the diffraction pattern and is referred to as the diffraction halo of a single exposure (see Khetan & Chiang, 1975). This halo is the Fourier transform of the plate if  $d=0$ , or if only one exposure has been recorded on the plate. Its radius is given by the highest frequencies in the photograph. Outside it, there is no light and therefore no fringes. It is therefore obvious that if the photograph contains only low frequencies, we cannot observe fringes due to small displacements, since they will be outside the halo. In other words, the displacement needs to be larger than the

width of the intensity peaks for the whole field filtering method.

In our case, the displacement is 40, and the peak width is 20. It will be shown in chapter four that there is an easily measurable difference between spectra obtained when  $d=40$ , and when  $d=41$ . Suppose that the width of the peak was 200 instead of 20. Then we would need to increase our displacement to at least 200, and try to measure a difference between fringe patterns produced by  $d=200$  and  $d=201$ .

The resolution is thus limited by the size of the peaks, which is in turn dependent on the atmosphere, film resolution and lens diameter and quality.

When a double exposure is made with a displacement  $d(d_x, d_y)$  between exposures, the halo is modulated by cosine square fringes. These can be seen if  $d$  is uniform over the whole field. If  $d$  is non-uniform, the corresponding fringes will have different spacings and orientations, and therefore no pattern will be seen. If a small aperture is placed in the transform plane at  $x_2$ , fringes will be observed in the image plane of another lens depicting different values of the component of  $d$  along  $x_2$ .

Dark fringes are obtained for

$$\cos[(k/2f)(d_x x_2 + d_y y_2)] = 0$$

or for

$$d_x x_2 + d_y y_2 = (n + 1/2)\lambda f \quad (3.19)$$

These fringes are the isothetics, that is, loci of points of equal displacement component. For example, if we are looking at the y-component of displacement of a disc under rotation, the fringes would appear as straight lines, parallel to the y-axis, with spacing between fringes given by the magnitude of the displacement component.

### 3.3 Pointwise filtering

A selected point on the photographic record is illuminated by a narrow beam of coherent light. The diffracted light can be observed by placing a plate of ground glass at some distance L from the photographic plate (figure 10). An accurate way to measure these fringes would be to replace the ground glass by a photographic plate and expose the fringe pattern directly on it. A microdensitometer could then be used to scan the fringes and the obtained curve could then be fitted by a least squares method to a curve of the form  $A(x)\cos^2 kx$ , where  $A(x)$  forms the envelope of the fringes. From the geometry of the figure, we have (see Khetan and Chiang, 1976):

$$\begin{aligned}
 r &= \{L^2 + [x_2 - (x_1 - \bar{x}_1)]^2 + [y_2 - (y_1 - \bar{y}_1)]^2\}^{1/2} \\
 &= L \left[ 1 + (x_2 + \bar{x}_1 - x_1)^2 / L^2 + (y_2 + \bar{y}_1 - y_1)^2 / L^2 \right]^{1/2}
 \end{aligned}$$

Taking the first two terms in the binomial expansion, (Fresnel approximation) we get:



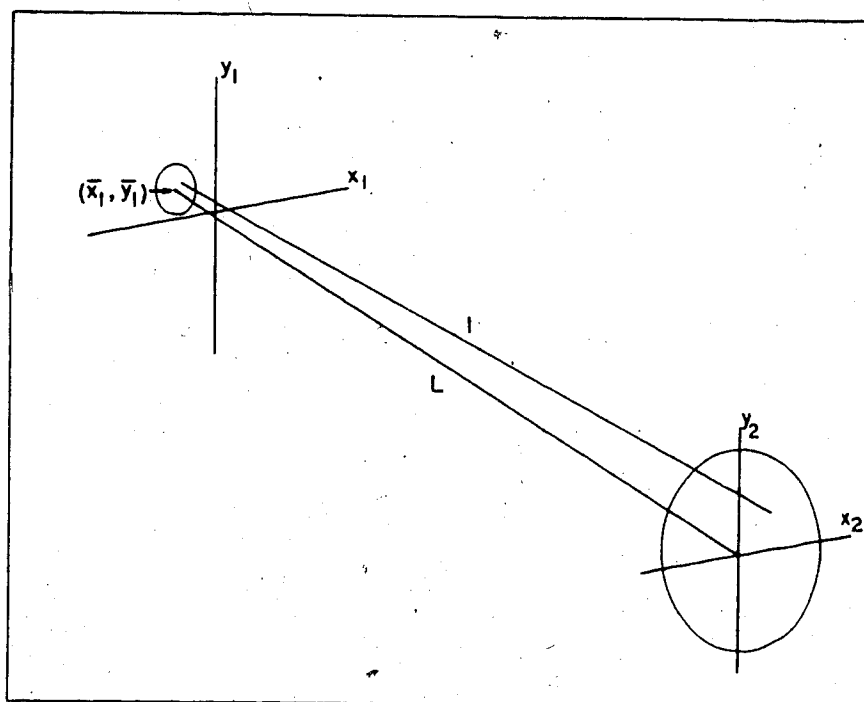


Figure 10.... Arrangement for pointwise filtering

$$l \approx L + (x_2^2 + y_2^2 + 2x_2\bar{x}_1 + 2y_2\bar{y}_1)/2L + ((x_1 - \bar{x}_1)^2 + (y_1 - \bar{y}_1)^2)/2L - (x_2x_1 + y_2y_1)/L \quad (3.20)$$

The intensity in the transform plane is:

$$I(x_2, y_2) = \left| \iint g'(x_1, y_1) \exp(ikl) dx_1 dy_1 \right|^2 \quad (3.21)$$

The first two terms in equation (3.20) will give a phase factor, and can be dropped. We can assume that except near the center of the diffraction halo,

$$(x_2x_1 + y_2y_1)/L \gg ((x_1 - \bar{x}_1)^2 + (y_1 - \bar{y}_1)^2)/2L \quad (3.22)$$

(This is again the Fraunhofer approximation, therefore we are again dealing with Fraunhofer diffraction).

Inserting equation (3.20) into equation (3.21), we get:

$$I(x_2, y_2) = \left| \iint_{\substack{\text{beam} \\ \text{size}}} g'(x_1, y_1) \exp[ik(x_2x_1 + y_2y_1)/L] dx_1 dy_1 \right|^2 \quad (3.14 b)$$

which is identical to equation (3.14 a) except that the integration limits are given by the beam size rather than the aperture function. Then we have, as before,

$$I(x_2, y_2) = 4 I_1(x_2, y_2) \cos^2 [ (k/2L)(d_x x_2 + d_y y_2) ] \quad (3.18 b)$$

In this case, straight fringes can be seen even for an inhomogeneous deformation because within the limits of the

beam size, ( $\approx 1$  to 2 mm) the displacement field can be considered uniform. The fringes in this case are uniformly spaced straight lines, with spacing density proportional to the magnitude of the displacement vector, and orientation normal to the displacement vector. Pointwise filtering yields more accurate results than the whole field approach for the following reasons:

1. The fringes are equidistant and their spacing can therefore be averaged.
2. The fringes are sharper and more clearly defined.
3. No lenses are required, thus there are no errors due to lens aberrations.
4. A rigid body translation or rotation can be introduced to give some initial fringes, and change of fringe spacing can be measured, rather than the fringe spacing itself. If no rigid body displacement is introduced, the sensitivity is the same as for the whole field case.

If we have two peaks, they will be resolved (by Rayleigh's criterion) if  $d = b/1.22$ . Since the intensities of the peaks are added, we can't expect to get any fringes if the peaks are not resolved, therefore

$$d(\min) = b/1.22 \quad (3.23)$$

Using the whole field method, the smallest ground displacement we can therefore see is  $20/1.22 \approx 16$  centimeters. However, in the pointwise filtering approach,

we can add a small displacement to the photographs before they are exposed on a single plate, to make  $d$  about 40. When  $d=40$ , the Fourier transform obtained has clearly defined fringes, with a spacing measurably different from the fringes obtained when  $d=41$ . This means that a difference in ground displacement of 1 cm can be detected using the pointwise filtering method, but not the whole field method.

It is possible to digitize the interesting sections of the doubly-exposed plate, and measure the separations directly. This method would have the advantage that if the peaks were much wider than the expected 20 pixels, (a pixel is a picture element) and if they were too close to be resolved by Rayleigh's criterion, they could still be deconvolved (since we know their approximate shape), and their separation could be obtained. If the noise level is high, deconvolution filters may become unstable, and even this method will not work. Assuming however, that it is possible to get peak widths of 20 pixels or less, analysing the diffraction pattern would have the following advantages over direct measurement:

1. To obtain the diffraction pattern we need only pass a laser beam through the double exposure. The fringes can then be photographed, and their separation can be measured with a ruler, in the direction parallel to the fault direction. An error in direction of 5 degrees will introduce an error of less than 1/4 cm in the displacement of the reflector.

To do a direct measurement of peak separation, we need to use a microscope to enlarge each area and digitize the enlarged sections. This digitization needs to be done in two dimensions. The separation between the peaks can be found by cross correlation with a single peak.

2. Since fringes are equidistant, we can average over several fringes to get the average separation, or do a least squares fit of the fringes to a  $\cos^2$  curve. No such averaging is possible when we do a direct measurement.

If the noise level is very high, the direct measurement may work better, since the cross-correlation can still pick out the position of the peaks even if they are completely buried in random noise. The transform plane analysis has been chosen, because this method makes it unnecessary to digitize in two dimensions. Also, if sections of the original photograph are digitized, using a microscope and a microdensitometer, and the separations are found using the direct comparison method, we can perform the digital Fourier transform, and analyse the digitally-obtained fringes. This way, we will be able to compare the results obtained by direct measurement, and by analysing the transform plane.

In the next chapter, we will assume that  $d=d$  and  $d=0$ , thus enabling us to do all computations in one dimension without any loss of generality, and at one tenth the cost and storage space requirement. One example is done in two

dimensions to show that small shape changes do not affect the results.

### 3.4 The Discrete Fourier Transform

The calculations in chapter three were all done by the use of the continuous Fourier transforms, whereas in chapter four, the discrete Fourier transform has been calculated by the computer.

In one dimension, we can use a vector of 1000 points and perform the Fourier transform quite inexpensively. To extend the problem to two dimensions, we should first reduce the number of data points, since it would be impractical to use an array of 1000 by 1000 points. In order to reduce the data, we must first understand exactly how the computer calculates the discrete transforms. Normally, the Fourier series is developed independently of the Fourier integral. Here, we are interested how the discrete Fourier transform relates to the continuous one, therefore we will develop it as a special case of the continuous Fourier integral (Brigham, 1974). Consider the continuous function  $h(t)$ , and its Fourier transform  $H(f)$ , where  $t$  can stand for time or space, and  $f$  can be either temporal or spatial frequency (figure 11). We want a discrete Fourier transform pair which approximates the pair  $h(t):H(f)$ . First, we need to sample the function  $h(t)$ , by multiplying it by the Dirac comb, with sample interval  $T$ . The transform of the sampled function

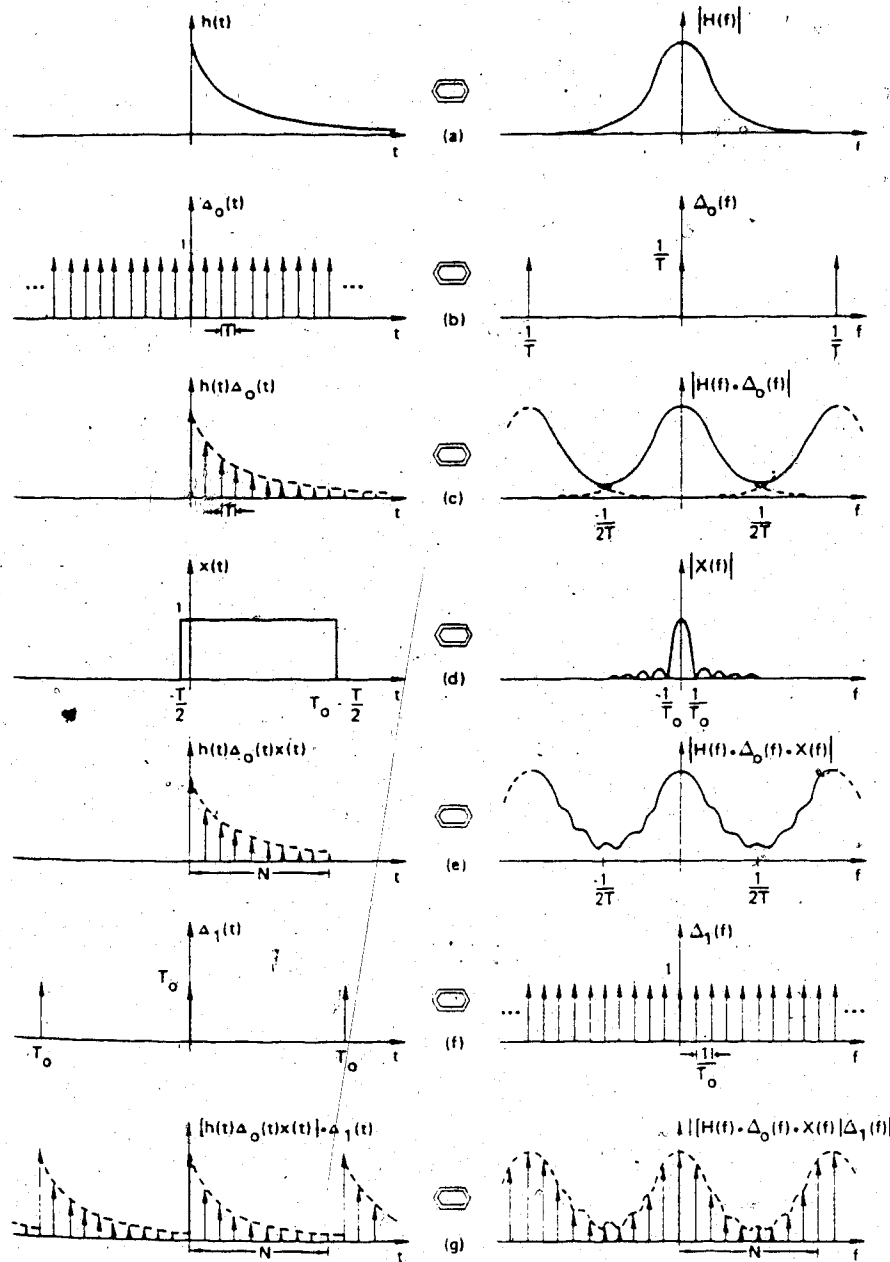


Figure 11.3. Development of the discrete Fourier transform pair: figure taken from Brigham, 1974, p95

$\hat{h}(t)$  is given by the convolution of  $H(f)$  and the transform of the Dirac comb (see Appendix for proof). Aliasing will modify the transform pair (as seen in figure 11(c)), if the sampling interval is chosen too large. If  $h(t)$  is band-limited, we can avoid aliasing error by choosing  $T \leq 1/2F$ , where  $F$  is the highest frequency component of  $H(f)$ .

So far, we have only considered an infinite number of samples of  $\hat{h}(t)$ . To be suitable for computation by computer, the function  $\hat{h}(t)$  has to be truncated by multiplication with a rectangle function  $x(t)$ , so that  $N$  samples are left. The resulting transform is shown in figure 11(e). As  $x(t)$  becomes very wide,  $X(f)$  approaches a delta function, and the ripple which has been added to the transform will be attenuated.

It is now necessary to modify the frequency transform by a frequency sampling function to make it suitable for machine computation. Just as the sampling in the time domain resulted in a periodic function of frequency, sampling in the frequency domain results in a periodic function of time. If the original function is approximated by  $N$  samples, the transform will also be approximated by  $N$  samples (figure 11(g)).

Under the following conditions, the discrete Fourier transform will be exactly equal to the continuous transform.

1.  $h(t)$  must be periodic
2.  $h(t)$  must be band-limited
3. Sampling interval must be smaller than  $1/2F$



4.  $x(t)$  must be non-zero over an integer multiple of exactly one period of  $h(t)$

The class of functions we are dealing with are of finite duration in space, and therefore cannot be band-limited, but they need not be truncated. Consider for example a triangle function (figure 12). In the next chapter, the peaks will be roughly gaussian in shape. Since the Fourier transform of a gaussian is again a gaussian, a triangular pulse will illustrate these ideas more clearly. The continuous transform is a  $\text{Sinc}^2$  function. The discrete transform may or may not resemble the continuous one, depending on the aliasing effect, which is determined by the sampling interval  $T$ , and depending on the spacing of the points in the frequency domain, which can be controlled by the number of zeros which we stick on the ends. In figure 12(a),  $N$ , the number of samples is 128, and no zeros are added. In figure 12(b),  $N$  is 16, with no zeros added, and in fig. 12(c), 16 samples are taken of the triangle, with the rest of the samples being zero, to give a total of 128.

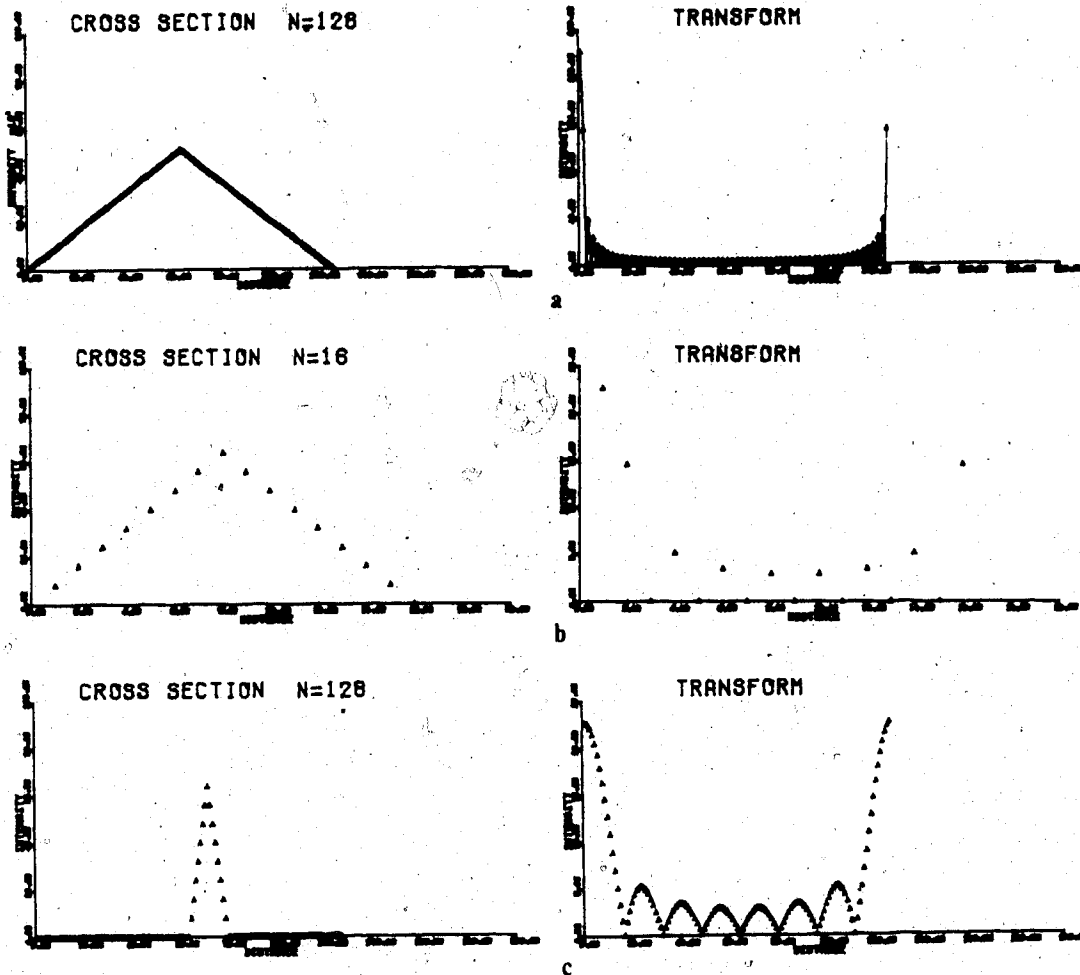


Figure 12.... A triangle function sampled at different rates, with its discrete Fourier transform on the right

#### 4. COMPUTATIONS WITH SYNTHETIC DATA

I do not have actual data, so in the following computations, the simulated cross sections of corresponding sections of 2 photographs were added together, giving the intensity distribution of a double exposure plate. The sections have a diameter of 1000 picture elements, or 1 millimeter, which is about the diameter of a laser beam used to illuminate the section. The double exposure is then Fourier transformed, to give the intensity in the frequency plane. Since one picture element on the photograph corresponds to 1 cm on the ground, the laser beam covers an area with diameter about 10 meters, and containing only one light. The computations therefore simulate the pointwise filtering approach described earlier. Maximum resolution is possible when the width of the peak (b) equals one. As the peak approaches a delta function, the radius of the halo approaches infinity, and since the fringes are equidistant, we can measure the separation between a large number of fringes, thus greatly reducing the error. As the halo radius approaches infinity, the bright fringes approach a constant intensity. (figure 1)

Diffraction patterns were obtained for  $d=40, 25, 10$  and  $3$ , (figure 2) and a graph of (fringe separation) versus the displacement  $d$  has been made (figure 3). It is linear, as predicted by equation 3.19.

Next, we will look at more realistic intensity distributions, that is, peaks of finite width. In chapter two, preliminary calculations showed that it is possible to

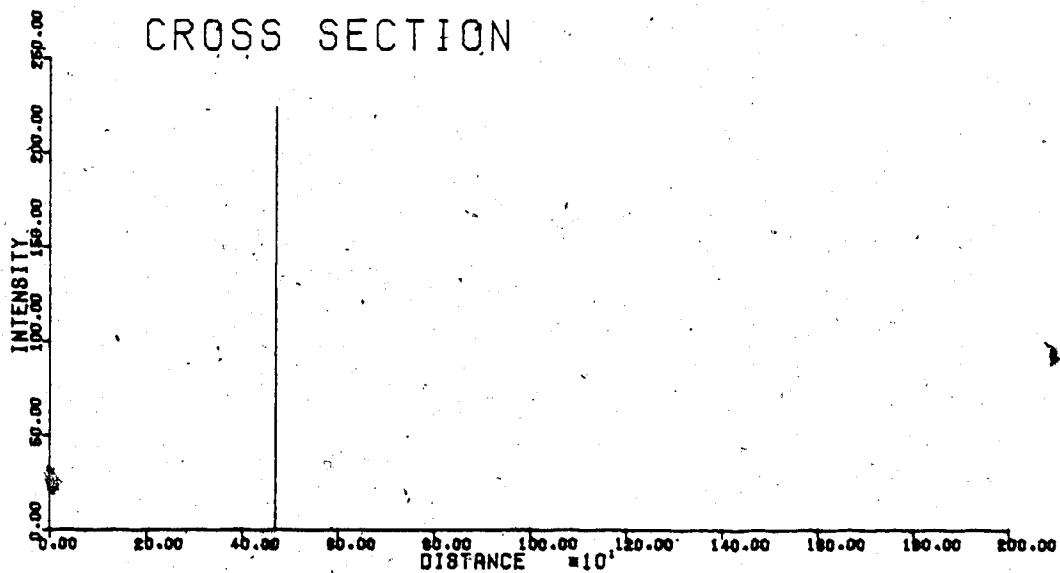
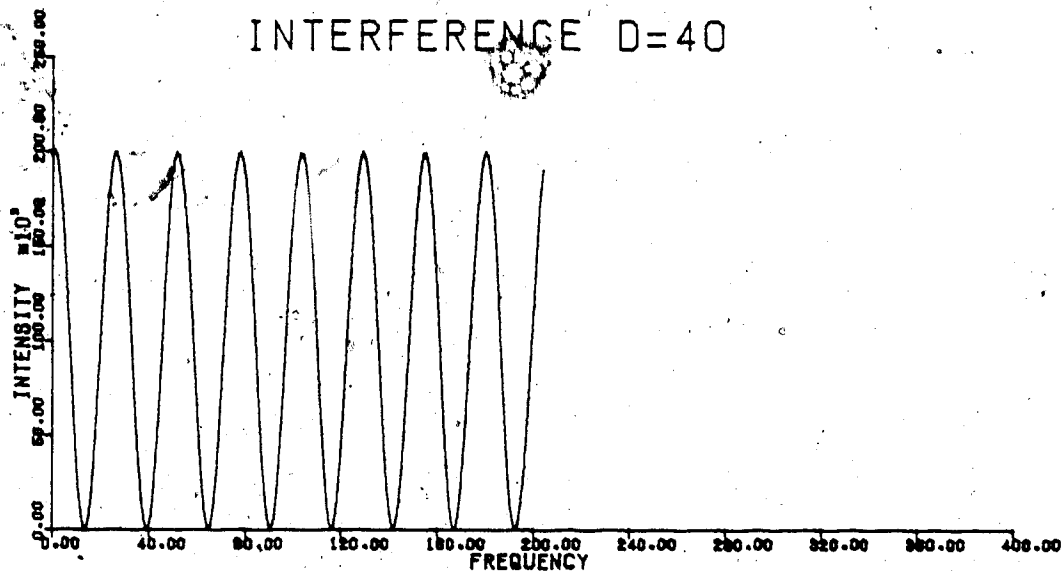


Figure 13.... For a peak of width 1, fringes extend to infinity

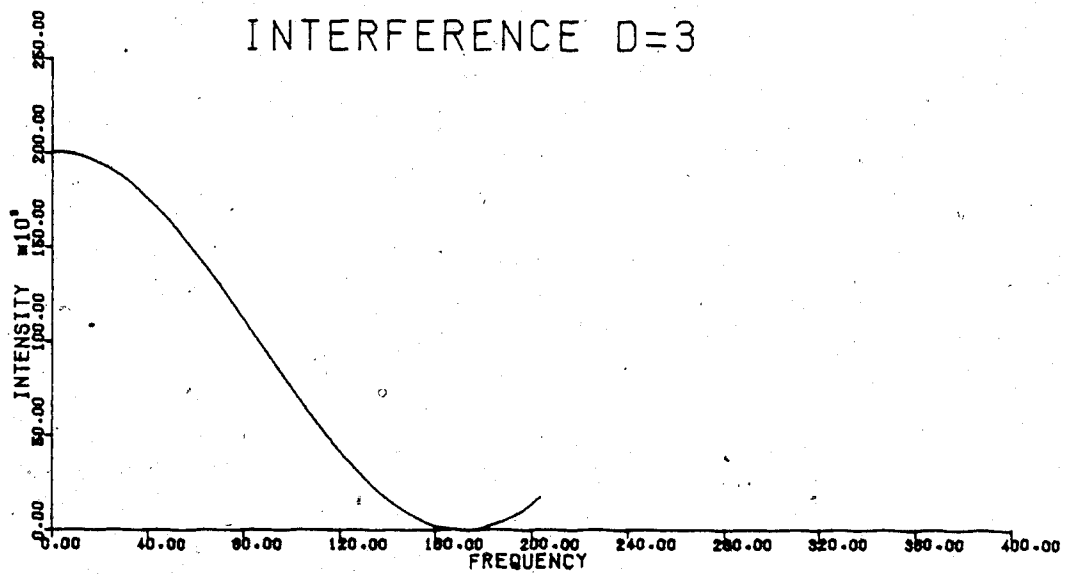
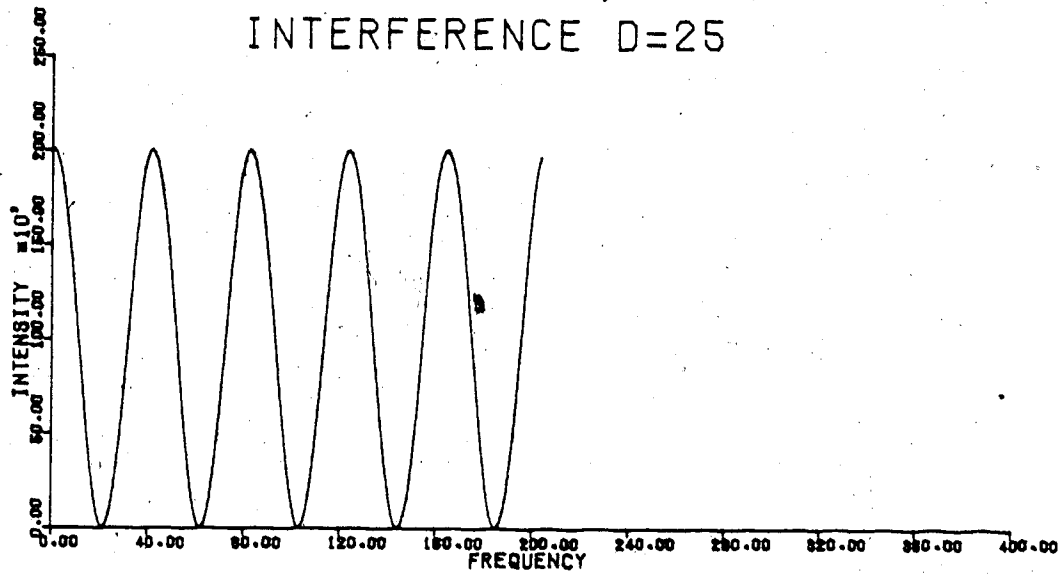


Figure 14.... Displacement is inversely proportional to the fringe separation

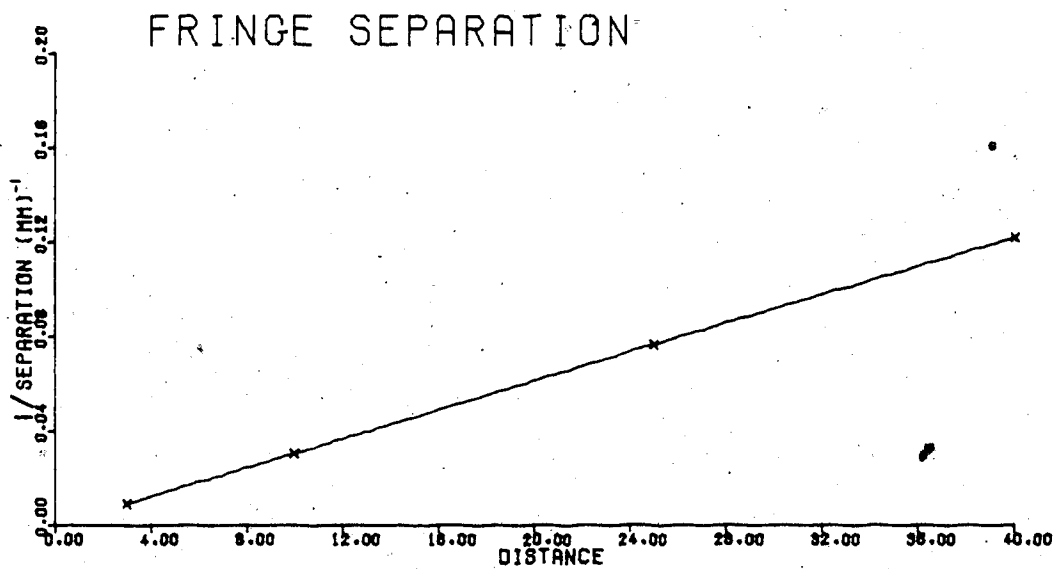


Figure 15.... Calibration graph showing inverse relationship between fringe separation and distance between the peaks

obtain peaks of a width of  $b \approx 20$ . A displacement  $d=0$  is equivalent to a single exposure, and therefore shows only the diffraction halo (figure 16). For a delta function, a displacement  $d=2$  produces a clearly visible fringe pattern. In the case of a finite-width peak, however, fringes are not visible, until the displacement is larger than  $d(\text{min})$  given by equation 3.23. Since the intensities of the two peaks are added, we only expect fringes if the total intensity distribution looks like two peaks, and not one (figure 17). The diffraction pattern produced by  $d=40$  is not clearly different from one obtained when  $d=41$  or  $42$ , but the difference can be measured using a ruler (figure 18).

The next step is to add random noise to each photograph (figure 19). The signal to noise ratio is about 10:1 and the fringes are still clearly visible. Using a digital band-pass filter subroutine written by Dave Ganley (see Appendix), the high frequency noise was filtered out. In an optical system, band-pass filtering is a very easy process, as was shown in chapter two. Unfortunately, the visibility of fringes was not improved at all (figure 20). The same results were obtained when the signal to noise ratio was reduced to 2:1 (figure 21) and (figure 22).

The importance of peak width has already been discussed in the previous chapter. The diffraction halo, which forms an envelope containing the fringe pattern, decreases with increasing peak diameter (figure 23). The peak width in this figure is about 50.

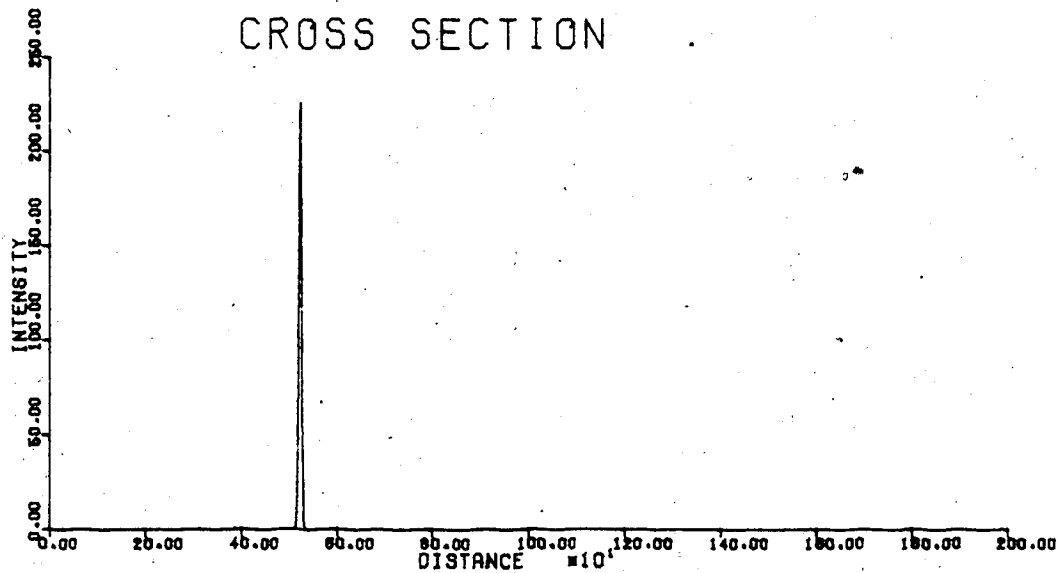
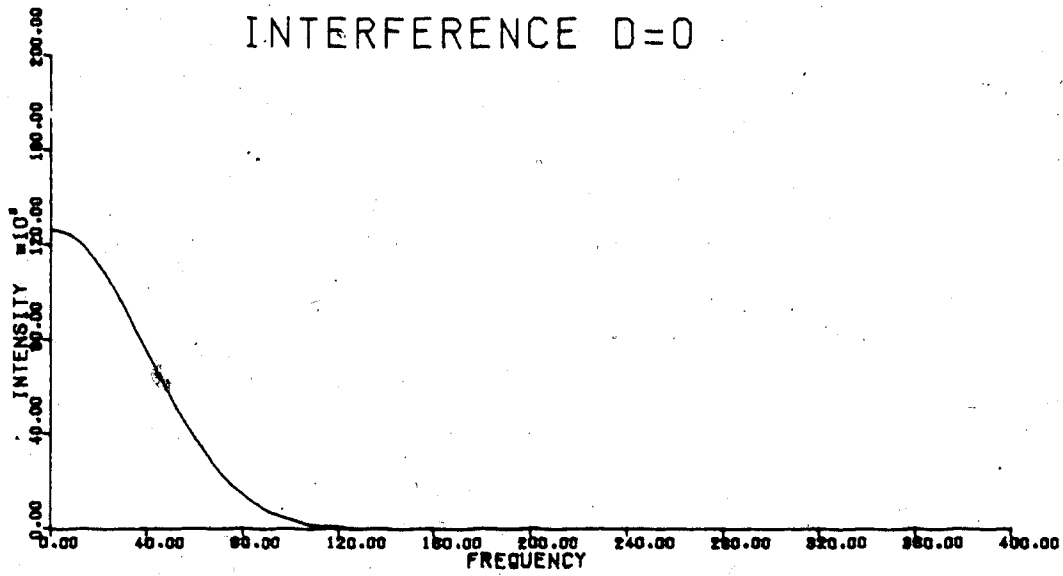


Figure 16.... A displacement of  $d=0$  produces the diffraction halo, the frequency distribution due to a single peak



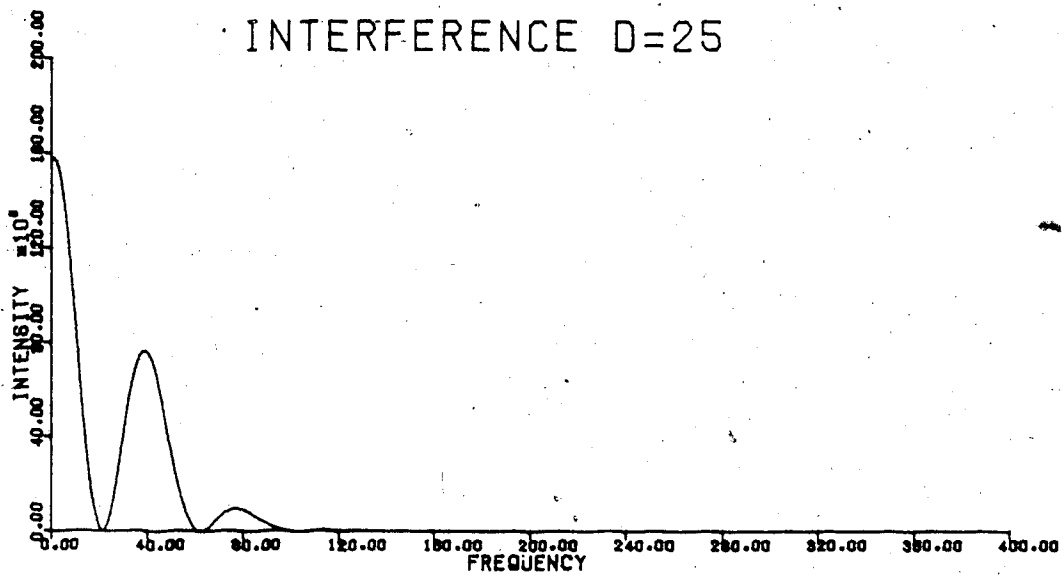
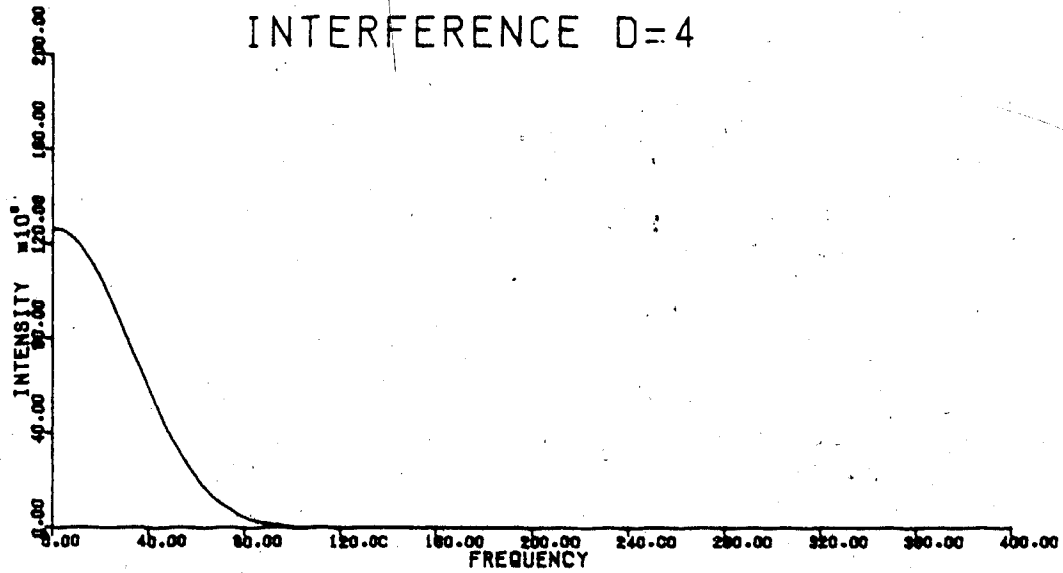


Figure 17.... Fringes become visible only when  $d > 16$ , as predicted by equation 3.23

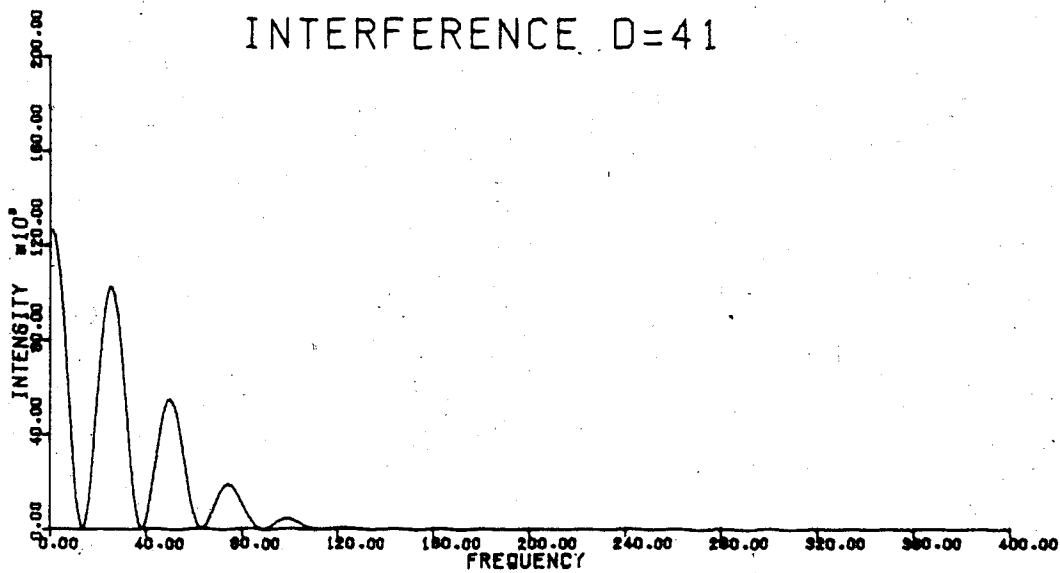
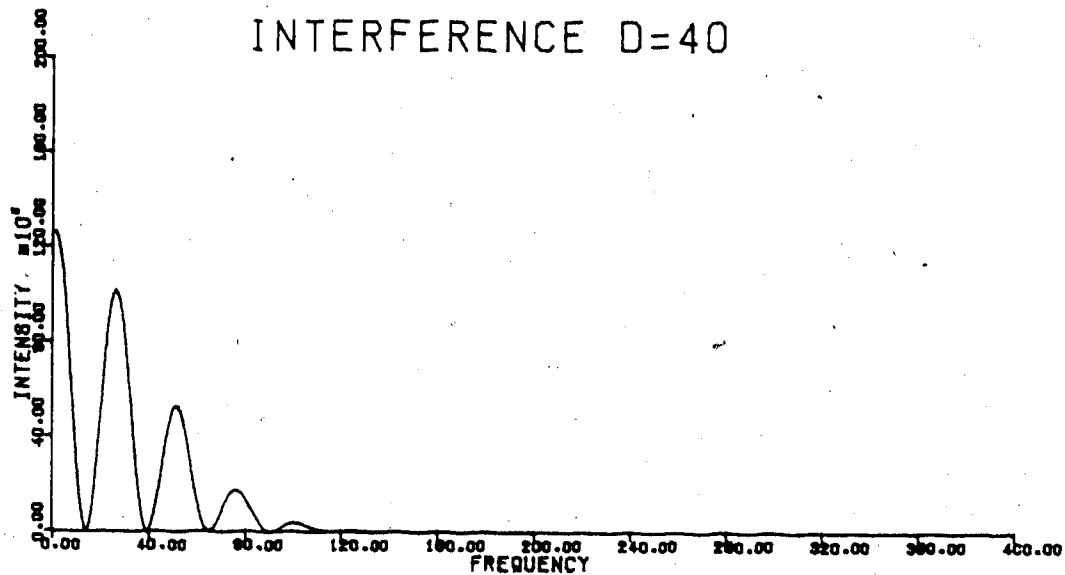


Figure 18.... Differences in diffraction patterns for  $d=40$  and  $d=41$  can be easily measured with a ruler

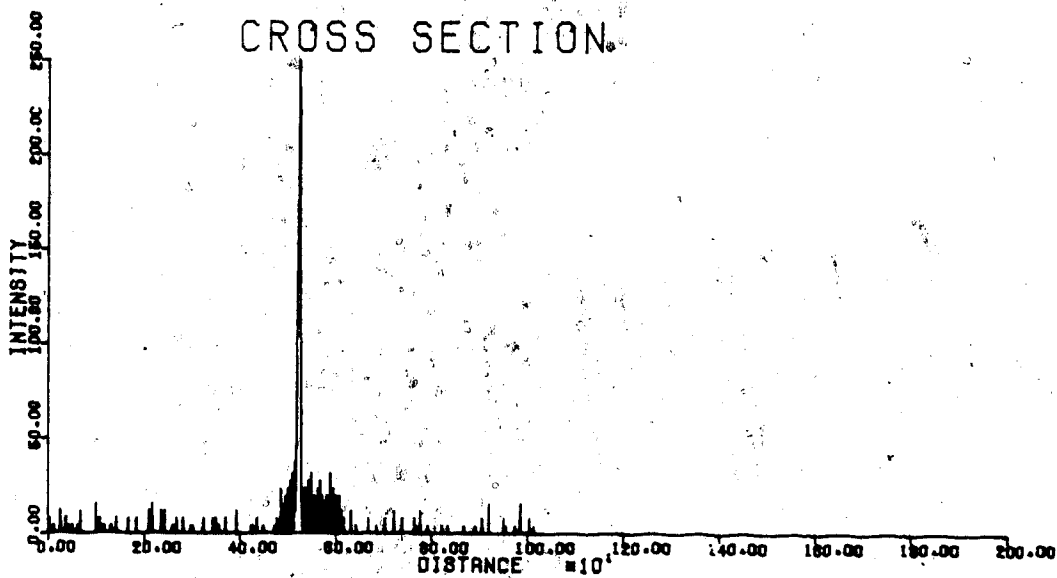
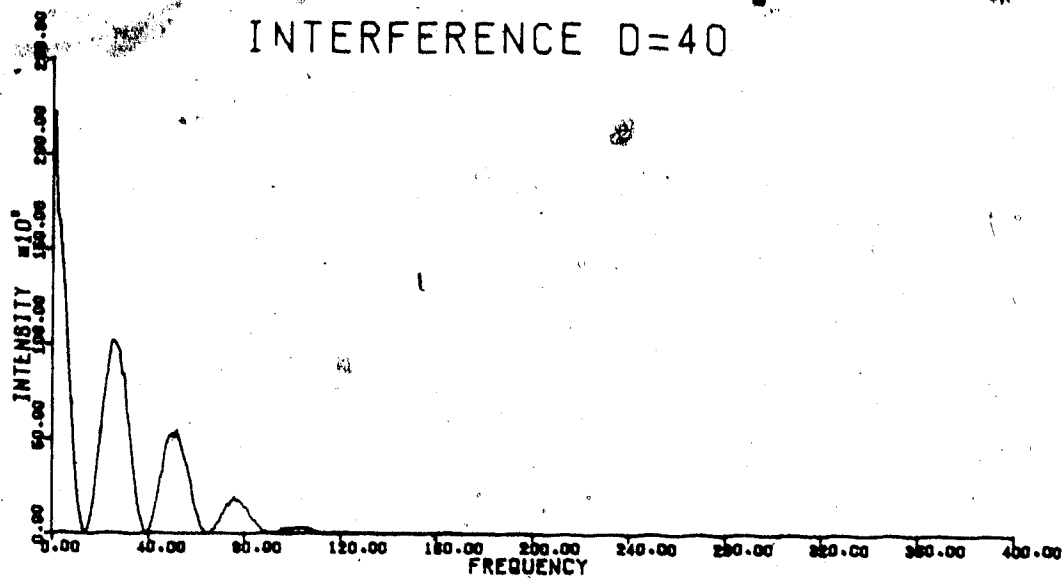


Figure 19.... Fringes are still clearly visible when random noise is added to the signal

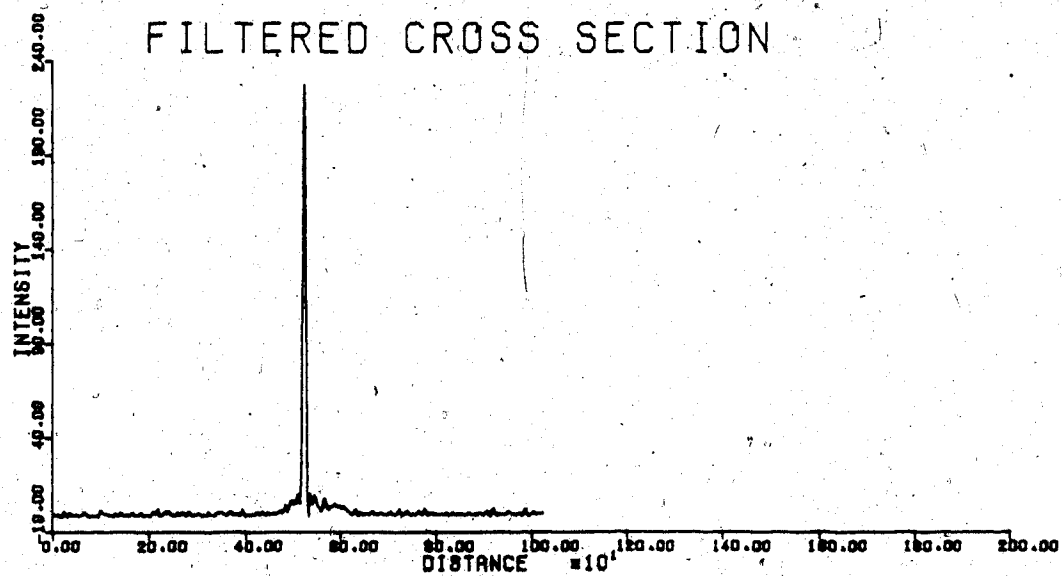
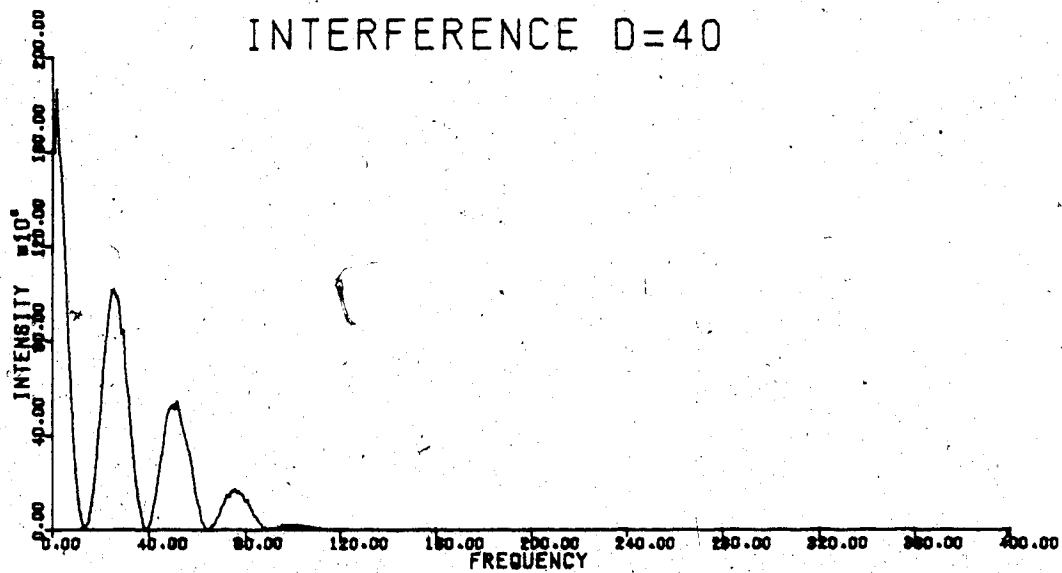


Figure 20.... Amplitude of noise has been reduced by band-pass filtering, with no significant improvement in the visibility of fringes

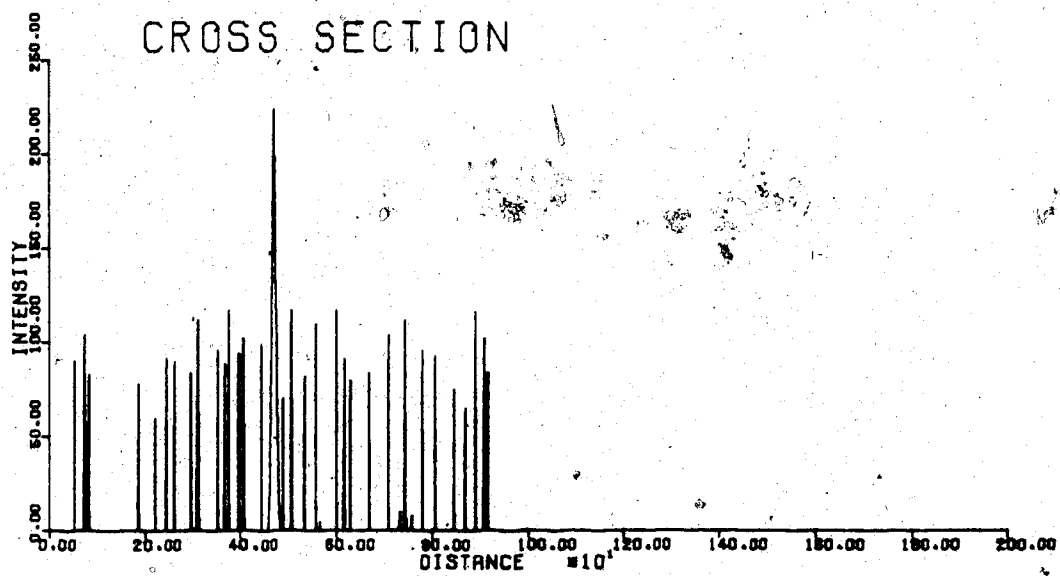
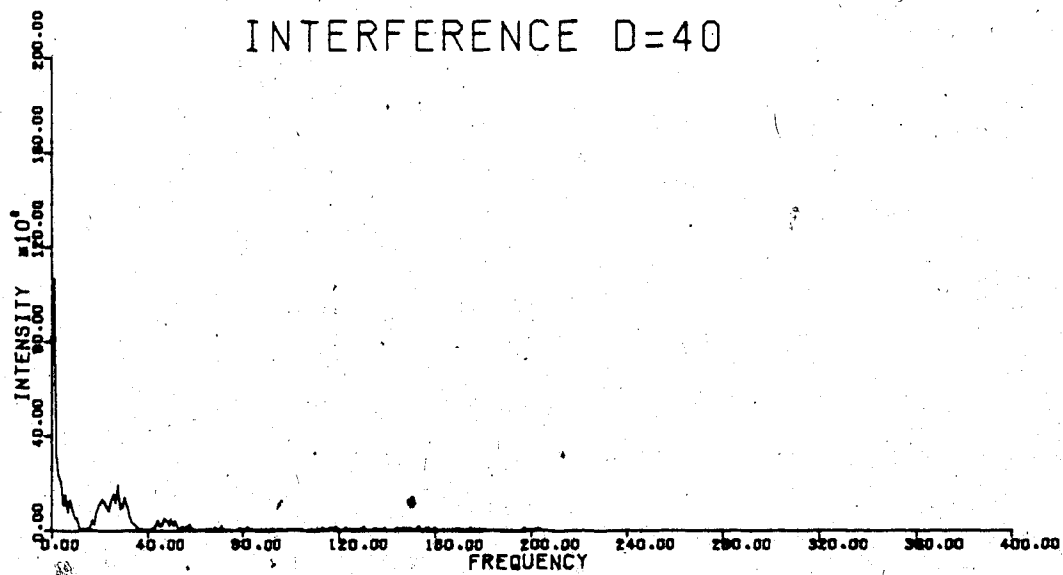


Figure 21.... Signal to noise ratio is reduced; fringes are still visible

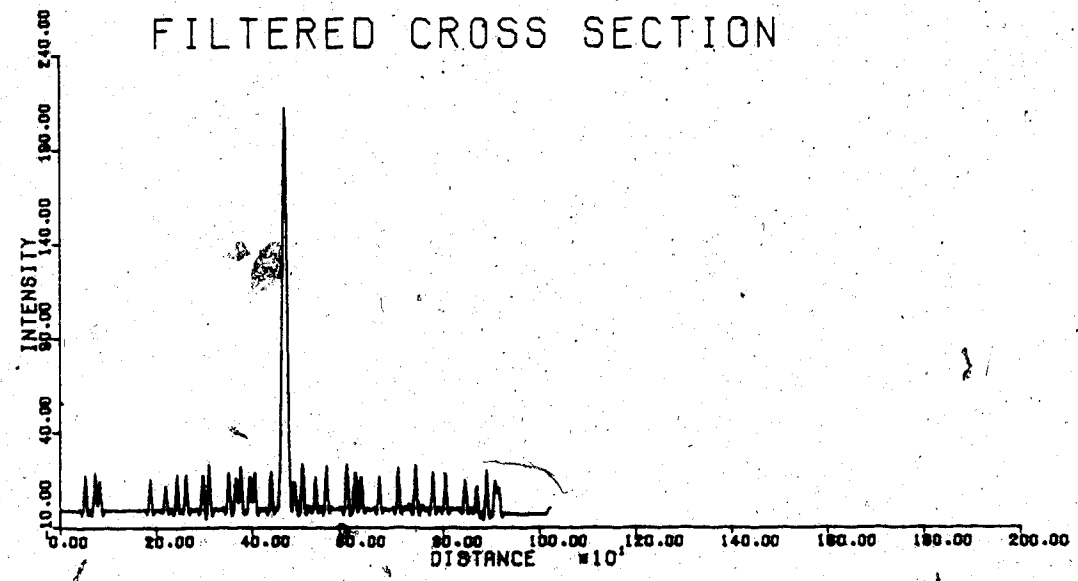
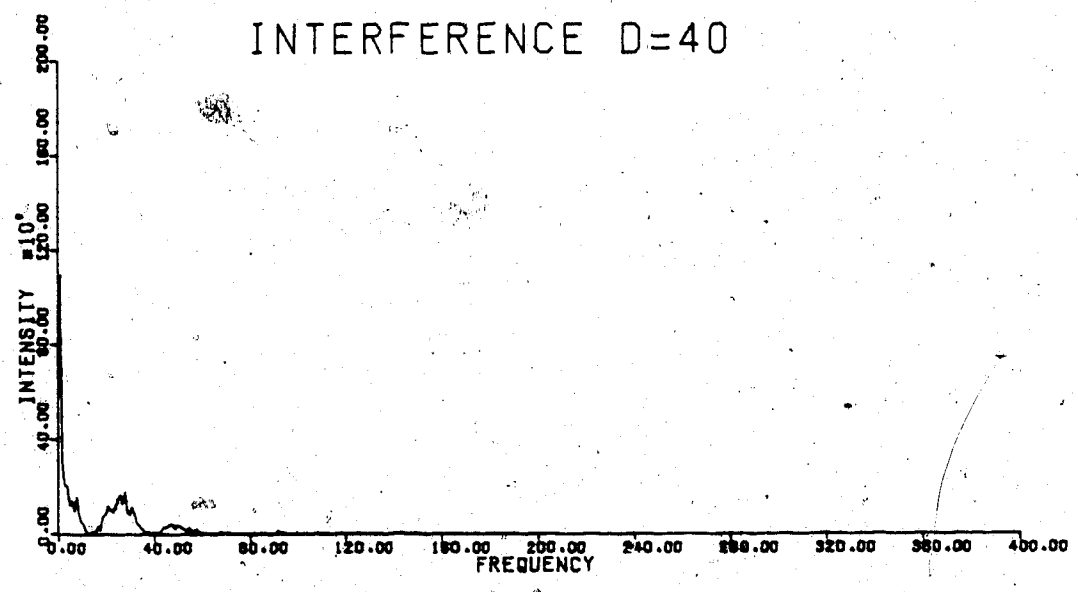


Figure 22.... At high noise level, band-pass filtering again has no effect on fringe visibility

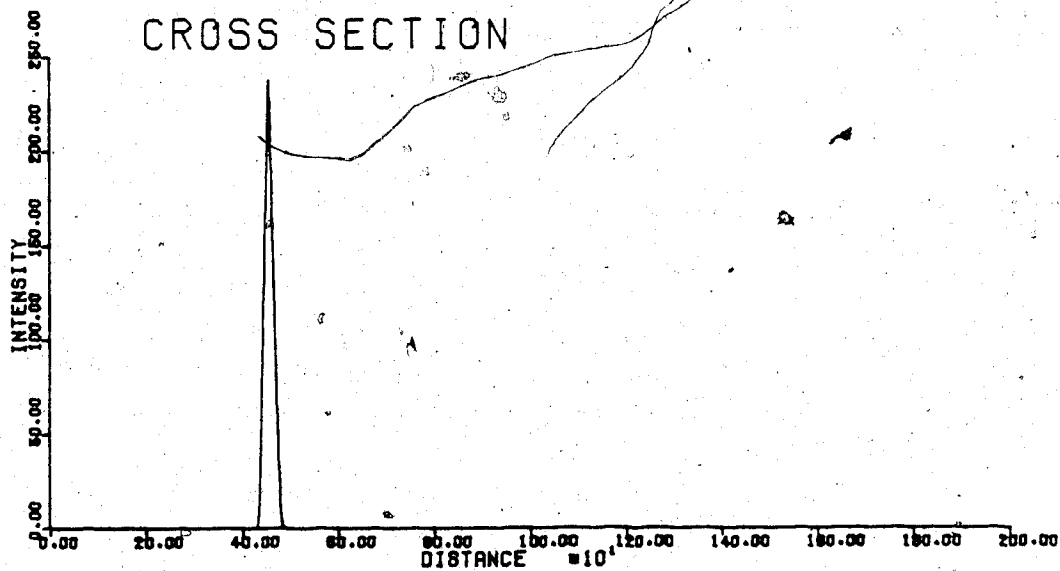
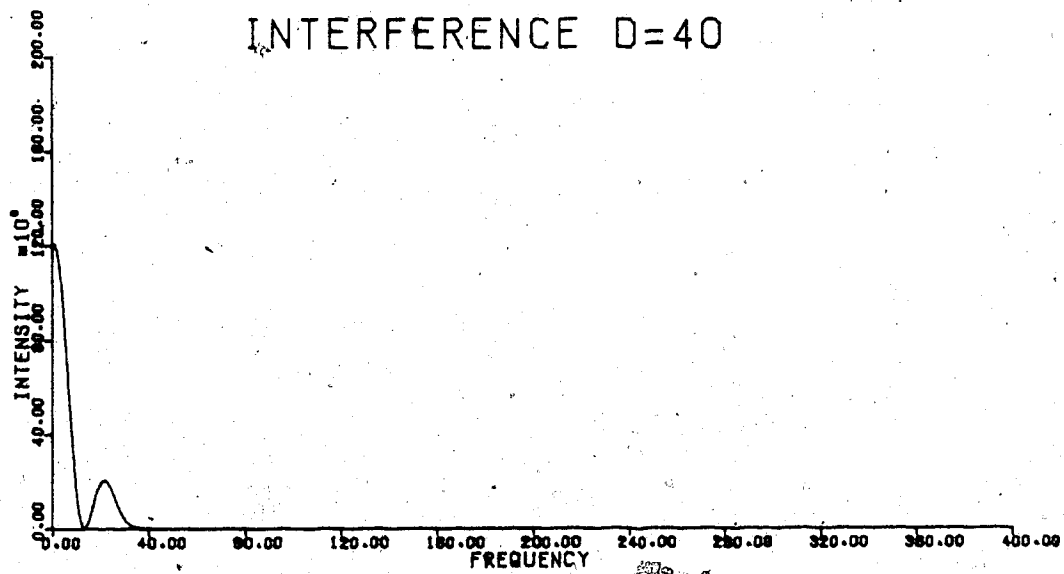


Figure 23.... Radius of the diffraction halo decreases with increasing peak width. In this figure, the peak is 50 lines wide.

It is to be expected that the width of the peak will not be the same on two pictures which are taken at different times. If one peak is wider than the other, the size of the halo will be limited by the size of the wider peak (figure 24). In this figure, one peak had a width of 18 and the second about 50. Out of the photographs taken, we hope to have about twenty good quality photographs for each year. These will be paired up such that we are comparing photographs containing spots of similar sizes. Thus comparing two peaks with a width ratio of 3:1 would occur only in the worst possible case. The error introduced by this asymmetry is easy to calculate from figure 24. The fringe separation is inversely proportional to the distance between the peaks, where the constant of proportionality is  $32.8 \text{ cm}^2$  (calculated from figure 13 or 14). The mean fringe separation in figure 24 is  $(.80 \pm .04) \text{ cm}$ . This gives a ground displacement of  $41 \pm 2 \text{ cm}$ ; the actual displacement used was  $40 \text{ cm}$ . The error is large, not because of the asymmetry, but because one peak was three times the maximum acceptable width, and because only  $1/2$  of a diffraction halo was measured. In the actual experiment, we will have about 20 full diffraction patterns, and the error should thus decrease by a factor of  $\sqrt{40}$ .

Clearly, it is undesirable to have two peaks in one section, since this will give a superposition of two sets of fringes. If the separation of the lights is much greater than  $d$ , the superposition will resemble a beat pattern,



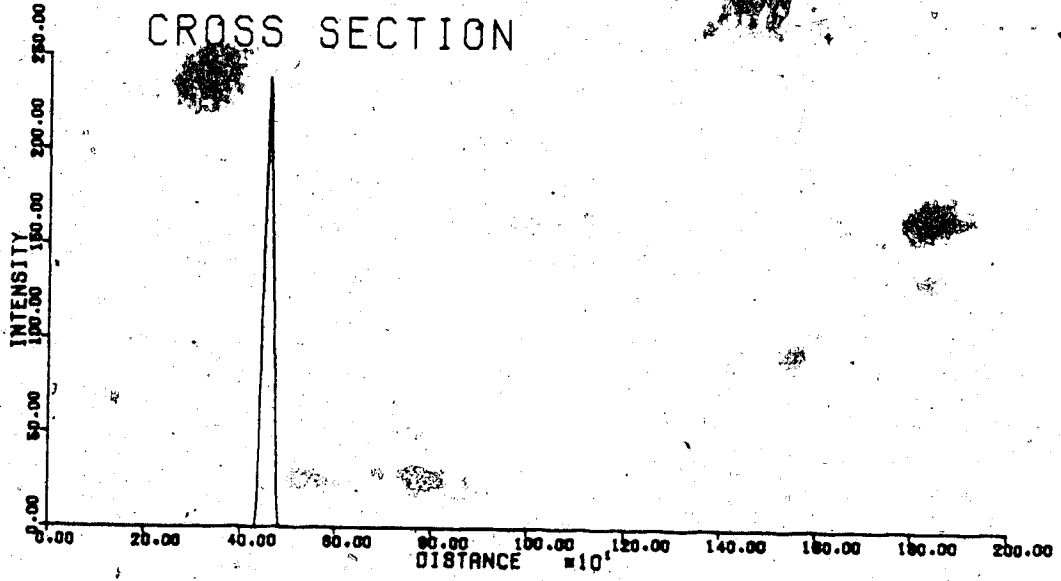
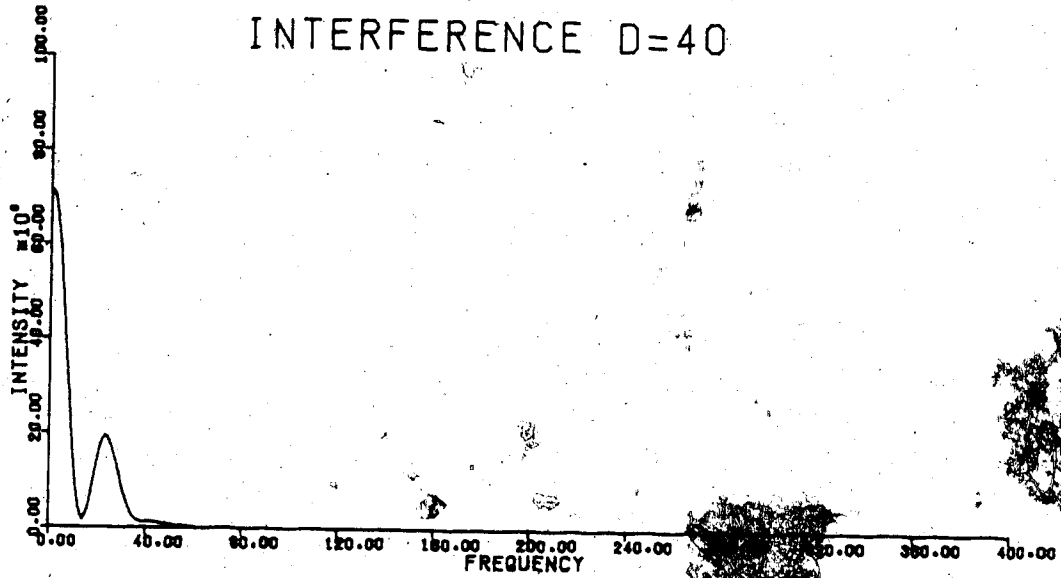


Figure 24.... If one peak is wider than the other, the size of the halo is limited by the width of the wider peak: width of peak shown is 50, other peak has a width of 18

(figure 25) and a less enlightening pattern is obtained if the distance between them is almost equal to the displacement, or if the displacement is different for peak.

If we have a large number of randomly spaced lights in the area, then our experiment approaches that of Khetan and Chiang. The fringe pattern obtained is quite noisy, and resembles the pattern obtained for two peaks. (figure 26). This is probably because the pattern is not completely random, but it is obvious that an interferogram obtained with a large number of peaks will not have fringes as clearly defined as that obtained using just one peak.

From figure 16, we know that the maximum frequency is about 120, so the sampling interval used was much finer than necessary. The number of data points can thus be reduced from 1024 to 128 before aliasing problems become significant. A simple extension of figure 18 to two dimensions has been done (figure 27). In this figure, the width of one peak is 20 pixels in the y direction and 24 in the x direction. The second peak is widest in the direction at  $45^\circ$  to the x axis.  $d_x=48$ , and  $d_y=40$  ( $|d|=62.48$  at  $39.8^\circ$  to the x axis). The figure was drawn on an electrostatic printer/plotter, using 16 different dot sizes.

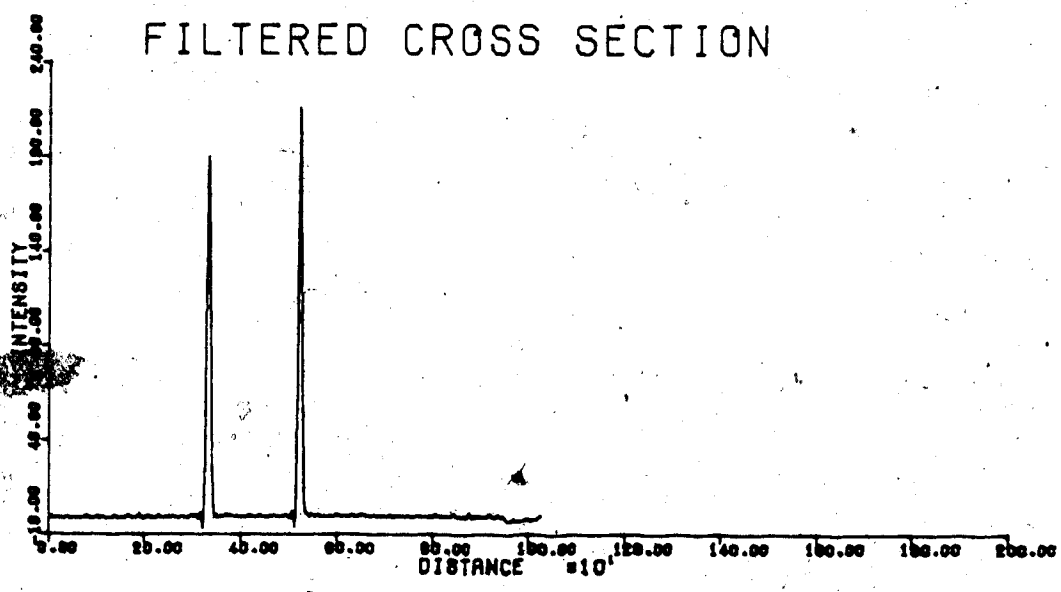
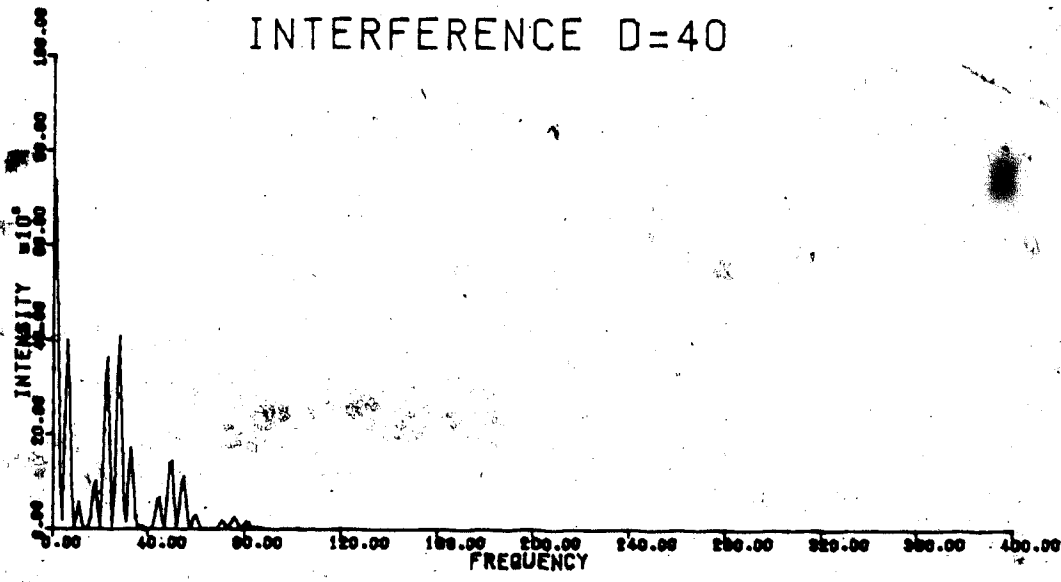


Figure 25.... A beat pattern is observed if two lights are present in one section

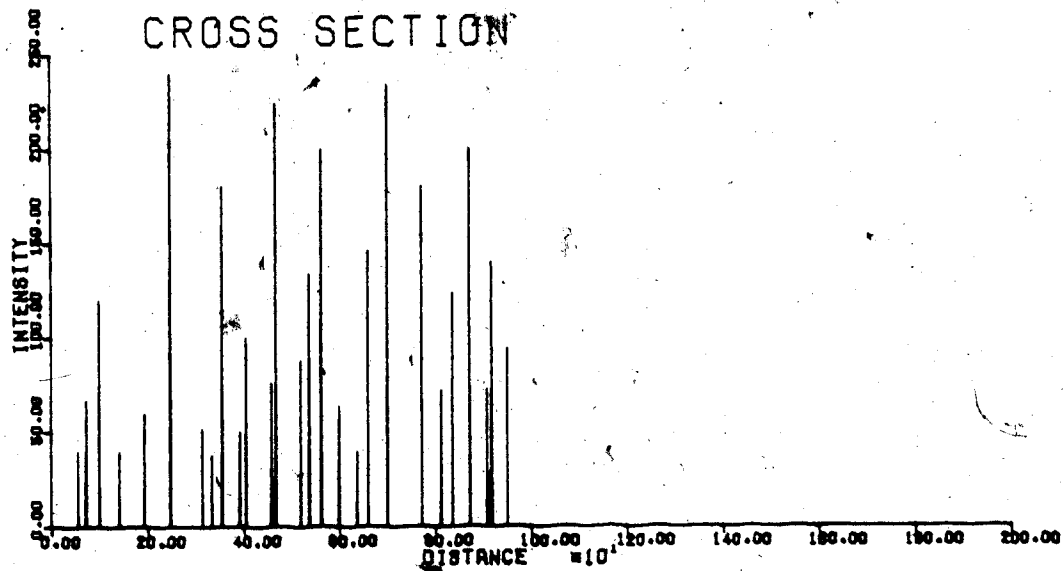
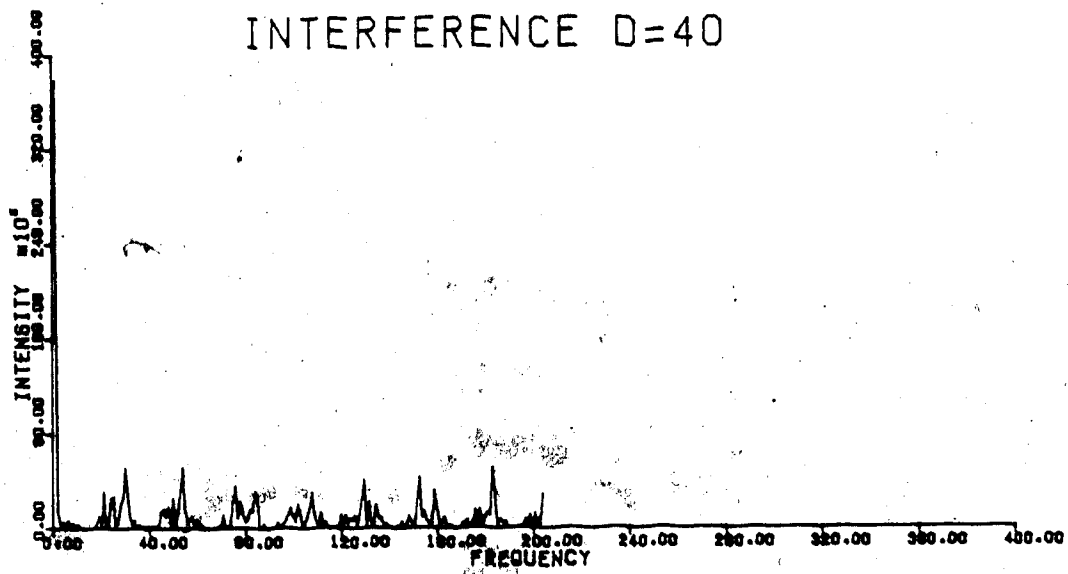


Figure 26.... Interference pattern obtained from a random pattern of delta functions

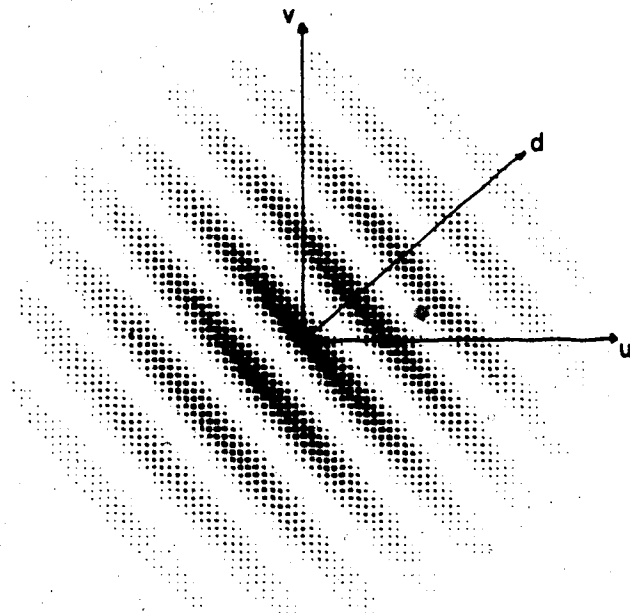


Figure 27.... Density plot of a diffraction pattern produced by 2 gaussian-shaped peaks showing the orientation and magnitude the displacement. The actual displacement was  $d=(48,40)$ .

## 5. CONCLUSION

It is only in the last decade that geodetic instrumentation and measurement techniques have reached the sophistication necessary to detect yearly surface deformation near active faults. Stress accumulation, which is always accompanied by surface deformation, is of major importance for understanding earthquake mechanisms.

Earthquakes occur when the accumulated stress reaches some critical value, called the failure stress. We proposed a method of determining surface strain rates in an area of small aperture (about 1 km). It was assumed that in an area 10 meters in diameter, the displacement will be uniform, and the area can therefore be represented by a single point. A row of lights (or reflectors) separated by 10 - 20 meters, and perpendicular to the fault, can thus be used to measure the cross section of yearly strain accumulation across the fault.

Using a rectangular array of reflectors, rather than a linear array will increase the amount of useful information. For example, if the surface strain distribution is linear across the fault, a linear array of reflectors will still look linear after it has been displaced. One cannot therefore distinguish between a real linear displacement distribution, and an apparent displacement caused by misalignment of the camera, or a horizontal temperature gradient. A rectangular array, on the other hand, will still appear rectangular if the camera is rotated, however it will

be parallelogram-shaped if the displacement is real. Due to the small displacements involved, I feel that it is unlikely that one could recognize the difference between a parallelogram and a rotated rectangle.

Preliminary calculations in chapter two were based on parameters set by commercially available terrestrial cameras or phototheodolites (camera combined with a theodolite). Several models are available from both Wild and Zeiss Canada. Some significant characteristics of these models are:

1. Picture formats vary from 60 by 80 mm to 130 by 180 mm. on photographic plate, or cut and roll film.
2. Lens distortion, camera frame and photographic plate or film produce a combined error no greater than .008 mm.
3. Focal lengths range from 45 to 200 mm.
4. Focal length to object distance should be kept down to 1:3000.
5. Prices start at \$7000 (in 1976)

It has been shown that a measurable difference exists in the interference patterns produced by a reflector which was displaced by 40 cm, and one displaced by 41 cm. Non-uniform displacements of the order of 1 cm can therefore be detected. To distinguish between real displacements, and apparent displacements caused by the atmosphere, we can concentrate on points close to the main axis, which eliminates error due to vertical refraction index gradient, and we can neglect the small effect of a horizontal

gradient. Rapid atmospheric fluctuations are removed by long period averaging, achieved by long exposure times (one minute or more). Slow fluctuations can be minimized by monitoring the weather conditions.

The most important result obtained is that by introducing a small initial displacement, the sensitivity of the system has been increased by a factor of about 20. That is, if the smallest detectable displacement using a direct comparison is  $b/1.22$ , where  $b$  is the width of the narrowest peaks in the photograph, then using the method described earlier, the smallest detectable displacement is  $1/20$  of  $b/1.22$ . At the same time, the problems encountered in a direct comparison, such as misalignment, are avoided in this method, since the initial displacement can be unknown.

### 5.1 Suggestion for geophysical experiment

The field set-up of the experiment is shown in figure 8. A terrestrial camera is used to image an array of lights a distance  $h$  below. The light sources could be a set of reflectors, with one powerful light source somewhere below the camera, and well out of sight from the camera's position. Using reflectors will allow us to carry out the experiment at night, under less turbulent atmospheric conditions. Reflectors can be left in the field over long periods of time, and they will work again when needed, without having to be located first. The power needed for the



single light source will be much greater than the combined power which would be needed if all reflectors were replaced by battery-powered light sources, however due to the large number of reflectors proposed for this experiment, using light sources would not be economically feasible.

The reflectors should be close to the main axis, to minimize the effect of the vertical index of refraction gradient. They need not form any precise geometrical pattern. A "random" pattern such as in figure 8 is sufficient. The only constraint is that the reflectors lie in a band approximately 200 meters wide, centered on the main axis. The ultimate goal of the experiment is to overlap two photographs of these lights onto a single transparency. This will produce an array of light-pairs on a dark background. The separation and relative orientation of the two lights in each pair can then be determined by examining the interference pattern they produce when a laser beam is passed through them.

The experiment must be broken up into sections, and each part must be carefully tested before going on to the next. In the first case, the width of each light on the film must be kept to less than .02 mm. Theoretically, this can be easily achieved using a film with resolution of 1000 lines/mm, and a  $f/1.2$  lens. The light source will produce a bright spot on the transparency. The width of the spot can be easily obtained by inspecting the Fraunhofer diffraction produced when we pass a laser beam through the spot. The

film must be properly developed to get peaks of this width.

This test should be repeated now with a large distance between the light source and camera, to simulate the atmospheric conditions. The required peak width should again be less than .02 mm. Here, it is important to have a lens with diameter of 5 cm or more.

Once the double exposure has been obtained, and the separations between the peaks in every pair have been measured, the separations can be graphed as a function of the peaks' perpendicular distance from the fault. Before graphing the results, we must remove the displacement due to camera alignment. To do this, we will assume that the closest reflector has not moved with respect to the camera, and that the camera is in exactly the same position, but may have been rotated slightly.

Using the model of Turcotte and Spence (1974, equation 6) one could do a least squares fit to the data, to find the rate of strain accumulation, and the depth below which the plates slip freely.

The errors in the position of the reflector images are due to the atmosphere, camera alignment, and plate stability limitations. The errors due to the atmosphere are most troublesome, because of their variability. As was found by Vacquier and Whiteman, a large percentage of the photographs are unusable because of unfavorable atmospheric conditions during exposure.

Photographic plates should be stable to within .01%. A 10 cm plate should therefore be stable to 10 microns. Testing plate stability can be done in the lab, as the first step in determining the practical feasibility of this method.

The camera cannot be aligned precisely as it was one or two years before. This unfortunately limits our method to detection of non-linear displacement fields.

The ideas behind this experiment are very simple, but to actually carry out the whole experiment will require a great deal of care and patience. The method seems feasible theoretically, and this work should be taken into its next stage, which is to determine the practical feasibility.

## BIBLIOGRAPHY

- Adams, C. the Array Processor - An Answer in Search of a Scientist's Question [SPIE Vol. 149, Digital Image Processing, (1978)]
- Archbold, E. and Ennos, A.E. Displacement Measurements from Double Exposure Laser Photographs [Opt. Acta, 19, 253, (1972)]
- Bender, P.L., and Owens, J.C., Correction of Optical Distance Measurements for the Fluctuating Atmospheric Index of Refraction, [J. Geophys. Res. 70, 2461-2462, (1965)]
- Beynon and Lamb, *Charge-coupled Devices and their Applications* [McGraw-Hill, (1980)]
- Biedermann, K. Silver Halide Photographic Materials [Topics in Appl. Phys. Vol. 20, Holographic Recording Materials, (1977)]
- Brigham, E.O., *The Fast Fourier Transform* [Prentice-Hall, (1974)]
- Buffington, A. & al. Active Image Restoration with a Flexible Mirror [Spie, Vol. 75, Imaging through the Atmosphere.]
- Burch, J.M., & al. Holography with a Scatter Plate as Beam Splitter and a Pulsed Ruby Laser as Light Source [Nature, Vol. 212, (1966)]

Burnside, C.D., *Electromagnetic Distance Measurement* [Crosby Lockwood & Son Ltd, London, (1971)]

Castleman, K.R., *Digital Image Processing*, [Prentice-Hall, (1979)]

Chiang, F.P. and Juang, R.M. Laser Speckle Interferometry for Plate Bending Problems [Appl. Opt. 15, 2199, (1976)]

Considine, P. and Profio, A. Image Processing with In-line Optical Systems [SPIE Vol 16, Image Info. Recovery (1968)]

Considine, P.S., Effects of Coherence on Imaging Systems [J. Opt. Soc. Am., 56, (1966), p1001]

Considine P.S., and Gonsalves, R.A. Optical Image Enhancement and Image Restoration [Topics in Applied Physics, Vol. 23 (1978) Cassasent, D ed.]

Darby, D. et.al, Strain Displacement Measurements for the June 8, 1980 Victoria, Mexico Earthquake, [American Geophysical Union, (1981)]

Fienup, J.R. Space Object Imaging Through Turbulent Atmosphere [SPIE, Vol. 149, Digital Image Processing, (1978)]

Fried, D.L. Optical Resolution through a Randomly Inhomogeneous Medium for Very Long and Very Short Exposures [ J. Opt. Soc. Am. 56, 1372 (1966)]

- Fried, D.L. Limiting Resolution Looking Down through the Atmosphere [J. Opt. Soc. Am. 56, 1380, (1966)]
- Goodman, W.J., *Introduction to Fourier Optics* [McGraw-Hill, (1968)]
- Hecht, E. and Zajac, A., *Optics*, [Addison-Wesley, (1976)]
- Horner, J.L. and Rycus, M.J. Restoration of Linearly Smeared Transparencies [SPIE Vol 16, Image Info. Recovery, (1968)]
- Huang, T.S., ed., *Picture Processing and Digital Filtering* [Topics in Applied Physics, Vol. 23 (1979)]
- Huggett, G.R. and Slater, L.E., Precision of Electromagnetic Distance Measuring Instrument for Determining Secular Strain and Fault Movement [Tectonophysics, 29, 19-27, (1975)]
- Jackson, J.D. *Classical Electrodynamics* [J. Wiley & Sons, N.Y., (1975)]
- Kanasewich, E.R., *Time Sequence Analysis in Geophysics* University of Alberta press (1975)]
- Khetan, R.P. and Chiang, F.P., Strain Analysis by One-beam Laser Speckle Interferometry. I: Single Aperture Method [Appl. Opt. 15 2205 (1976)]
- Krulikowski, S.J., Jr. & al, Coherent Optical Parallel

- Processing [Bendix Technical Journal, Vol 1, (1968)]
- Krulikowski, S.J., Jr., and Forrest, R.B., Coherent Optical Terrain-relief Determination Using a Matched Filter [Bendix Technical Journal, Vol.5, (1972). ]
- Lawrence, R.S. A Review of the Optical Effects of the Clear Turbulent Atmosphere [SPIE, Vol.75, 2, Imaging through the Atmosphere]
- Lecouteur, G.M. Performance Tests on a Selection of 100-element CCD's [BBC research department report no. BBC RD 1976/23, (1976)]
- Margrave, G.F. Microgeodesy and South American Tectonics [PhD Thesis, Geophysics, Physics, University of Alberta, (1980)]
- Nyland, E. & al, Measurement and Analysis of Ground Movement Using Microgeodetic Networks on Active Faults [Geofisica Internacional Vol 18: 1, p 53, Mexico, (1979)]
- Nyland, E. Repeated Geodetic Surveys as Experiments in Geophysics [The Canadian Surveyor, Vol.31, No.4, (1977)]
- Savage, J.C. and Kinoshita, W.T., Absence of Observable Geodetic Strain Accompanying Danville, California, Earthquake Sequence [Bulletin of Seismological Soc. Am., vol.61, No. 6, (1971)]
- Savage, J.C. and Prescott, W.H. Precision of Geodolite

Distance Measurements for Determining Fault Movements  
[JGR, vol. 78, No. 26, (1973)]

Savage, J.C and Wood, M.D. The Relation Between Apparent  
Stress and Stress Drop [Bull. Seism. Soc. Am. Vol. 61,  
No. 5, (1971)]

Slater, L.E., A Multi-Wavelength Distance Measuring  
Instrument for Geophysical Experiments [PhD thesis,  
University of Washington, (1975)]

Slater, L.E. and Hugget, G.R. A Multiwavelength  
Distance-measuring Instrument for Geophysical  
Experiments [JGR, Vol. 81, No. 35, (1976)]

Slepian, D. Linear Least Squares Filtering of Distorted  
Images. [J. Opt. Soc. Am. Vol. 57, (1967)]

Tatarski, V.I., *The Effects of the Turbulent Atmosphere on  
Wave Propagation* [Israel Prog. for Sci. Translations,  
Jerusalem, (1971)]

Thatcher, W., Strain Accumulation on the Northern San  
Andreas Fault Zone since 1906 [J. Geophys. Res. Vol. 80,  
p4873 (1975) ]

Turcotte, D.L. and Spence, D.A. An analysis of strain  
accumulation on a strike slip fault, [ Journal of  
Geophysical Research, 79, p4407 (1974)]

Vacquier, V. and Whiteman, R.E., Measurement of Fault



Displacement by Optical Parallax [JGR, Vol.78, No.5,  
(1973)]

Vest, C.M. *Holographic Interferometry* [Wiley Series in Pure  
and Applied Optics, (1979)]

Walters, D.L., and Kunkel, K.E., Atmospheric Modulation  
Transfer Function for Desert and Mountain Locations: The  
Atmospheric Effects on  $r$ . [J. Opt. Soc. Am. Vol.71,  
No.4, (1981)]

Walters, D.L., Atmospheric Modulation Transfer Function for  
Desert and Mountain Locations:  $r$ . Measurements [J. Opt.  
Am. Vol.71, No.4, (1981)]

Whittlesey, R. A High Resolution High Speed Film Scanner  
System Using Optically Butted Charge-Coupled Devices  
[SPIE Vol 149, Digital Image Processing, (1978)]

Yariv, A. *Optical Electronics* [Holt, Rinehart and Winston,  
(1976)]

Yellin, M. Using Membrane Mirrors in Adaptive Optics [SPIE,  
Vol.75, 97, Imaging through the Atmosphere]

## APPENDIX A: Notation

$f$ =focal length

$\lambda$ =wavelength of source ( $=2\pi c/\omega$ )

$P_1$ =object plane

$P_2$ =transform plane

$P_3$ =image plane

$(x_1, y_1)$ =point in  $P_1$

$(x_2, y_2)$ =point in  $P_2$

$(x_3, y_3)$ =point in  $P_3$ , inverted

$(u, v)$ =spatial frequencies in  $x$  and  $y$  directions respectively

$\vec{x}=(x, y)$ ,  $\vec{v}=(u, v)$

$i=\sqrt{-1}$

$i(x, y)$ =input

$o(x, y)$ =output

$p(x, y)$ =point spread function (impulse response)

Fourier transforms of functions are denoted by capital letters

$P(u, v)$ =optical transfer function (F.T. of point spread)

$s(x, y)$ =observed image

$n(x, y)$ =noise

$A(x, y)$ =aperture function

$I, O, P, S, N$  are Fourier transforms of  $i, o, p, s, n$  respectively

## APPENDIX B: Proofs of Fourier Transform Theorems

### Fourier Transform properties of lenses

Consider the input amplitude distribution  $g_1(x_1, y_1)$  in front of a spherical lens, with the observation plane a distance  $f$  behind the lens (see figure 5). From the Huygens-Fresnel principle, we have:

$$g(x, y) = \frac{\exp(ikd)}{i\lambda d} \iint_{-\infty}^{\infty} g_1 \exp\left[\frac{ik}{2d}((x-x_1)^2 + (y-y_1)^2)\right] dx_1 dy_1 \quad A1$$

where we used the approximations

$$\begin{aligned} \cos(n, r) &\approx 1 \\ r &\approx d \left[ 1 + \frac{(x-x_1)^2}{2d^2} + \frac{(y-y_1)^2}{2d^2} \right] \end{aligned}$$

and we ignore the finite size of the aperture. If the constant phase factor is dropped, then we have

$$\begin{aligned} g(x, y) &= \frac{1}{i\lambda d} \iint g_1(x_1, y_1) \exp\left[\frac{ik}{2d}((x-x_1)^2 + (y-y_1)^2)\right] dx_1 dy_1 \\ &= \frac{\exp\left[\frac{ik}{2d}((x^2 + y^2))\right]}{i\lambda d} \iint g_1 \exp\left[\frac{ik}{2d}((x_1^2 + y_1^2)) - \frac{ik}{d}(x_1 x + y_1 y)\right] dx_1 dy_1 \quad A2 \end{aligned}$$

similarly,

$$\begin{aligned} g_2(x_2, y_2) &= \frac{\exp\left[\frac{ik}{2f}((x_2^2 + y_2^2))\right]}{i\lambda f} \iint g' \exp\left[\frac{ik}{2f}((x^2 + y^2)) - \frac{ik}{f}(x_2 x + y_2 y)\right] dx dy \quad A3 \end{aligned}$$

substitute in for  $g'$  from equation 2.5

$$g_1(x_1, y_1) = \exp[(ik/2f)(x_1^2 + y_1^2)] / i\lambda f$$

$$\cdot \iint g(x, y) \exp[(-ik/f)(x, x+y, y)] dx dy \quad A4$$

$$= (\exp[(ik/2f)(x_1^2 + y_1^2)] / i\lambda f) G(u, v) \quad A5$$

where  $(u, v) = (x_1/\lambda f, y_1/\lambda f)$

$$G(u, v) = G_1(u, v) P(u, v) \quad (\text{from equation A1})$$

$$P(u, v) = \exp(ikd) \exp[-in\lambda d(u^2 + v^2)]$$

$$= \exp(ikd) \exp[(-ikd/2f^2)(x_1^2 + y_1^2)] \quad A6$$

$$G_1 = \iint g_1(x_1, y_1) \exp[(-ik/f)(x, x+y, y)] dx dy$$

therefore

$$g_1 = \exp[(ik/2f)(x_1^2 + y_1^2)(1 - d/f)]$$

$$\cdot \iint g_1(x_1, y_1) \exp[(-ik/f)(x, x+y, y)] dx dy \quad A7$$

Obviously, if  $d=f$ , the first exponential drops out and we are left with an exact Fourier transform relation.

#### Shift theorem

$$F\{g(x-a, y-b)\} = \iint g(x-a, y-b) \exp[-2\pi i(ux+vy)] dx dy$$

$$= \iint g(x', y') \exp[-2\pi i(u(x'+a)+v(y'+b))] dx' dy'$$

$$= \iint g(x', y') \exp[-2\pi i(ux'+vy')] dx' dy'$$

$$\cdot \exp[-2\pi i(ua+vb)]$$

$$= G(u, v) \exp[-2\pi i(ua+vb)] \quad A8$$

#### Convolution theorem

$$\text{If } G(u, v) = F\{g(x, y)\}$$

$$\text{and } H(u, v) = F\{h(x, y)\}$$

then

$$F\left\{\iint g(x', y') h(x-x', y-y') dx' dy'\right\}$$

$$\begin{aligned} &= \iint g(x', y') F[h(x-x', y-y')] dx' dy' \\ &= \iint g(x', y') \exp[-2\pi i(ux'+vy')] dx' dy' H(u, v) \\ &= G(u, v) H(u, v) \end{aligned}$$

### APPENDIX C: Programs

```

1  C .....
2  C
3  C
4  C
5  C
6  C
7  C
8  C
9  C
10 C
11 C
12 C
13 C
14 C
15 C
16 C
17 C
18 C
19 C
20 C
21 C
22 C
23 C
24 C
25 C
26 C
27 C
28 C
29 C
30 C
31 C
32 C
33 C
34 C
35 C
36 C
37 C
38 C
39 C
40 C
41 C
42 C
43 C
44 C
45 C
46 C
47 C
48 C
49 C
50 C
51 C
52 C
53 C
54 C
55 C
56 C
57 C
58 C
59 C
60 C
61 C
62 C
63 C
64 C
65 C
66 C
67 C
68 C
69 C
70 C
71 C
72 C
73 C
74 C
75 C
76 C
77 C
78 C
79 C
80 C
81 C
82 C
83 C
84 C
85 C
86 C
87 C
88 C
89 C
90 C
91 C
92 C
93 C
94 C
95 C
96 C
97 C
98 C
99 C
100 C
101 C
102 C
103 C
104 C
105 C
106 C
107 C
108 C
109 C
110 C
111 C
112 C
113 C
114 C
115 C
116 C
117 C
118 C
119 C
120 C

```

```

*****
S I P P R A C T I O N
*****
BY GEORGE KOVAR JANUARY 1968
THIS PROGRAM USES THE 2NDL FAST FOURIER TRANSFORM
TO OBTAIN THE SIPPRACTION PATTERN OBSERVED WHEN A
LASER BEAM PASSES THROUGH A PAIR OF PIN HOLES
DIMENSION Y(100),PTES0(100),W(100),PTES1(100)
* S I *
COMPLEX S(100)
DO 10 I=1,100
  S(I)=0
10 CONTINUE
DISPLACEMENT IN FRINGE UNITS IS EQUAL TO J*PI
READ(5,*)PTES0(J),J*PI,W(1),PTES0(J),J*PI,W(1)
20 FORMAT(10,10F4.0)
30 FORMAT(10,5F3.0)
CALL PLOT5
CALL PLOTY(PTES0,W)
CALL SYMBO(1,1,1,2,CROSS SECTION,1,0,10)
CALL SMOOTH(10,100,1,0.0)
CALL FILTER(PTES0,W,0.0,1)
CALL FILTER(PTES1,W,0.0,1)
CALL PLOT(1,1,1,2)
CALL PLOTY(PTES0,W)
CALL SYMBO(1,1,1,2,FILTERED CROSS SECTION,0,10)
DO 5 J=1,5
  PTES0(J)=PTES0(J)-PTES1(J)
  DO 10 I=1,100
    PTES0(I)=ABS(PTES0(I))
  10 CONTINUE
  C
  WRITE(6,*)PTES0(J),J*PI,W(1)
  CALL PLOT(1,1,1,2)
  DO 3 J=1,3
    PTES0(J)=ABS(PTES0(J))
  3 CONTINUE
  WRITE(6,*)PTES0(J),J*PI,W(1)
  CALL PLOT(1,1,1,2)
  N=2
  CALL PLOTY(PTES0,W)
  CALL SYMBO(1,1,1,2,INTERFERENCE PATTERN,0,10)
  CALL PLOT(1,0,100)
  RETURN
  END
C
SUBROUTINE PLOTY(Y,N)
BY G. KOVAR, JANUARY 1968
DIMENSION Y(100),X(100)
THE X COMPONENT IS INCREASED BY A CONSTANT INCREMENT
THE Y COMPONENT COMES FROM THE CALLING PROGRAM
STRAIGHT LINES ARE DRAWN BETWEEN ADJACENT POINTS
N IS THE NO OF DATA POINTS
40 FORMAT(10,5F3.0)
DO 10 I=1,N
  X(I)=1
  CALL PLOT(1,1,1,2)
  CALL SCALE(10,N,1)
  CALL SCALE(10,N,1)
  CALL AXIS(0,0,INTENSITY,0.0,0.00, Y(N+1),Y(N+1))
  IF (N.LT.1000)GO TO 75
  CALL AXIS(0,0,DISTANCE,0.10,0.0, X(N+1),X(N+1))
  GO TO 75
75 CALL AXIS(0,0,FREQUENCY,0.10,0.0, X(N+1),X(N+1))
75 CALL SING(1,Y,N,1,0.0)
  N=N+2
  WRITE(6,*)Y(1),101,N2)
  RETURN
  END
C
SUBROUTINE SBPAS(F1,F2,DELTA,B,S)
BY DAVE EARLEY QU MARCH 5, 1977
THIS SECTION CALCULATES THE FILTER AND MUST BE CALLED BEFORE
FILTER IS CALLED
F1 = LOW FREQUENCY CUTOFF (0 TO INFINITY)
F2 = HIGH FREQUENCY CUTOFF (0 TO INFINITY)
DELTA = SAMPLE INTERVAL IN MILLISECONDS
B = WILL CONTAIN 6 I DOMAIN COEFFICIENTS OF RECURSIVE FILTER
S = WILL CONTAIN THE GAIN OF THE FILTER.
WRITE (6,1) F1,F2,DELTA
1 FORMAT (1) BANDPASS FILTER DESIGN FOR A BAND FROM F1, F2 TO F2
3, HERTZ, SAMPLE INTERVAL IS DELTA, MILLISECONDS
DT=DELTA/1000.0
TDT=2.0/DT
PTB=4.0/DT
10W=1
P1=CMPLX(-.322634,.3226795)
P2=CMPLX(-.322634,-.3226795)
P3=CMPLX(-.3226795,.322634)
P4=CMPLX(-.3226795,-.322634)
W1=TWOP1+P1
W2=TWOP1+P2
W1=TDY+TAN(W1/TDT)
W2=TDY+TAN(W2/TDT)
NW1=(W2-W1)/2.0
WWW1=W2
DO 10 I=1,4
  Z1=P(I)-NW1
  Z2=Z1-WW
  Z2=CBRT(Z2)
  S(I)=Z1-Z2
10 CONTINUE
WRITE (6,2) S
2 FORMAT (1) S PLANE POLES ARE AT S(1),S(2),S(3),S(4)

```

```

181      36 M=3
182      M1=2
183      M2=1
184
185      37 XC(M)=XM-XM2-D(1)*XC(M1)-D(2)*XC(M2)
186      XD(M)=XC(M)-XC(M2)-D(3)*XD(M1)-D(4)*XD(M2)
187      XE(M)=XD(M)-XD(M2)-D(5)*XE(M1)-D(6)*XE(M2)
188
189      38 X(I)=XE(M)-XE(M2)-D(7)*X(I-1)-D(8)*X(I-2)
190      C
191      FILTER IN REVERSE DIRECTION
192      XM2=X(M)
193      XM=X(M-1)
194      XC(1)=XM2
195      XC(2)=XM1-D(1)*XC(1)
196      XC(3)=XM-XM2-D(1)*XC(2)-D(2)*XC(1)
197      XD(1)=XC(1)
198      XD(2)=XC(2)-D(3)*XD(1)
199      XD(3)=XC(3)-XC(1)-D(3)*XD(2)-D(4)*XD(1)
200      XE(1)=XD(1)
201      XE(2)=XD(2)-D(5)*XE(1)
202      XE(3)=XD(3)-XD(1)-D(5)*XE(2)-D(6)*XE(1)
203      X(N)=XE(3)
204      X(N-1)=XE(2)-D(7)*X(N)
205      X(N-2)=XE(3)-XE(1)-D(7)*X(N-1)-D(8)*X(N)
206      DO 49 I=4,N
207      XM2=XM1
208      XM=X(I)
209      J=N-I+1
210      XM=X(J)
211      K=1-(I-1)/3+3
212      GO TO (44,45,46),K
213
214      44 M=1
215      M1=3
216      M2=2
217      GO TO 47
218
219      45 M=2
220      M1=1
221      M2=3
222      GO TO 47
223
224      46 M=3
225      M1=2
226      M2=1
227
228      47 XC(M)=XM-XM2-D(1)*XC(M1)-D(2)*XC(M2)
229      XD(M)=XC(M)-XC(M2)-D(3)*XD(M1)-D(4)*XD(M2)
230      XE(M)=XD(M)-XD(M2)-D(5)*XE(M1)-D(6)*XE(M2)
231
232      48 X(J)=XE(M)-XE(M2)-D(7)*X(J+1)-D(8)*X(J+2)
233      IF (IG.NE.1) RETURN
234      DO 50 I=1,N
235      50 X(I)=X(I)/G
236      RETURN
237      END
238      G=.5/HWID
239      G=G*G
240      G=G*G
241      DO 29 I=1,7,2
242      S=-2.0*REAL(S(I))
243      Z1=S/I)*S(I+1)
244      G=REAL(Z1)
245      AC=DT+S*C/TDT
246      G=G*A
247      D(I)=(C-DT-FDT)/A
248      D(I+1)=(A-2.0*S)/A
249      G=G*G
250      RETURN
251      ENTRY FILTER(X,N,D,G,IG)
252
253      C
254      X = DATA VECTOR OF LENGTH N CONTAINING DATA TO BE FILTERED
255      D = FILTER COEFFICIENTS CALCULATED BY SNOFAS
256      G = FILTER GAIN
257      IG = 1 MEANS TO REMOVE THE FILTER GAIN SO THAT THE GAIN IS UNITY
258
259      C
260      IF (ISW.EQ.1) GO TO 31
261      WRITE (6,6)
262      6 FORMAT ('SNOFAS MUST BE CALLED BEFORE FILTER')
263      CALL EXIT
264      APPLY FILTER IN FORWARD DIRECTION
265
266      31 XM2=X(1)
267      XM=X(2)
268      XM=X(3)
269      XC(1)=XM2
270      XC(2)=XM1-D(1)*XC(1)
271      XC(3)=XM-XM2-D(1)*XC(2)-D(2)*XC(1)
272      XD(1)=XC(1)
273      XD(2)=XC(2)-D(3)*XD(1)
274      XD(3)=XC(3)-XC(1)-D(3)*XD(2)-D(4)*XD(1)
275      XE(1)=XD(1)
276      XE(2)=XD(2)-D(5)*XE(1)
277      XE(3)=XD(3)-XD(1)-D(5)*XE(2)-D(6)*XE(1)
278      X(1)=XE(3)
279      X(2)=XE(2)-D(7)*X(1)
280      X(3)=XE(3)-XE(1)-D(7)*X(2)-D(8)*X(1)
281      DO 33 I=4,N
282      XM2=XM1
283      XM=X(I)
284      XM=X(I)
285      K=1-(I-1)/3+3
286      GO TO (34,35,36),K
287
288      34 M=1
289      M1=3
290      M2=2
291      GO TO 37
292
293      35 M=2
294      M1=1
295      M2=3
296      GO TO 37

```